PEA15 loss of function and defective cerebral development in the domestic cat

Emily C. Graff[1,4,5,¶*], J. Nicholas Cochran[2,¶], Christopher B. Kaelin[2], Kenneth Day[2], Heather L. Gray-Edwards[3,4], Rie Watanabe[1], Jey W. Koehler[1,5], Rebecca A. Falgoust[4], Jeremy W. Prokop[2], Richard M. Myers[2], Nancy R. Cox[3,4], Gregory S. Barsh[2], Douglas R. Martin[3,4,5]; 99 Lives Consortium[‡]

Affiliations:

[1]Department of Pathobiology, College of Veterinary Medicine, Auburn University, Auburn, Alabama, USA

[2]HudsonAlpha Institute for Biotechnology, Huntsville, AL, USA

[3]Department of Anatomy Physiology and Pharmacology, College of Veterinary Medicine, Auburn University, Auburn, Alabama, USA

[4]Scott-Ritchey Research Center, College of Veterinary Medicine, Auburn University, Auburn, Alabama, USA

[5]Center for Neuroscience Initiative, Auburn University, Auburn, AL, USA

*Corresponding author: Correspondence should be addressed to Emily Graff (ecg0001@auburn.edu), Doug Martin (martidr@auburn.edu), or Greg Barsh (gbarsh@hudsonalpha.org).

[¶]These authors contributed equally to this work.

[‡]See Acknowledgements for list of members

Abstract

Cerebral cortical size and organization are critical features of neurodevelopment and human evolution, for which genetic investigation in model organisms can provide insight into developmental mechanisms and the causes of cerebral malformations. However, some abnormalities in cerebral cortical proliferation and folding are challenging to study in laboratory mice due to the absence of gyri and sulci in rodents. We report an autosomal recessive allele in domestic cats associated with impaired cerebral cortical expansion and folding, giving rise to a smooth, lissencephalic brain, and that appears to be caused by homozygosity for a frameshift in *PEA15* (phosphoprotein expressed in astrocytes-15). Notably, previous studies of a *Pea15* targeted mutation in mice did not reveal structural brain abnormalities. Affected cats, however, present with a non-progressive hypermetric gait and tremors, develop dissociative behavioral defects and aggression with age, and exhibit profound malformation of the cerebrum, with a 45% average decrease in overall brain weight, and reduction or absence of the ectosylvian, sylvian and anterior cingulate gyrus. Histologically, the cerebral cortical layers are disorganized, there is substantial loss of white matter in tracts such as the corona radiata and internal capsule, but the cerebellum is relatively spared. RNA-seq and immunohistochemical analysis reveal astrocytosis. Fibroblasts cultured from affected cats exhibit increased TNFα-mediated apoptosis, and increased FGFb-induced proliferation, consistent with previous studies implicating PEA15 as an intracellular adapter protein, and suggesting an underlying pathophysiology in which increased death of neurons accompanied by increased proliferation of astrocytes gives rise to abnormal organization of neuronal layers and loss of white matter. Taken together, our work points to a new role for *PEA15* in development of a complex cerebral cortex that is only apparent in gyrencephalic species.

Key Words: cat; autosomal recessive; neurodevelopment; PEA15; lissencephaly; sulci; gyri

Summary

Gyrification is the neurodevelopmental process in certain mammalian species during which the cerebral cortex expands and folds resulting in the classic wrinkled appearance of the brain. Abnormalities in this process underlie many congenital malformations of the brain. However, unlike many other human malformations, genetic insight into gyrification is not possible in laboratory mice because rodents have a lissencephalic or smooth cerebral cortex. We identified a mutation in domestic cats that likely causes failure of the cerebral cortex to expand and fold properly, and discovered that the mutation impairs production of a protein, PEA15 (phosphoprotein expressed in astrocytes-15), involved in intracellular signaling. Affected cats have profound abnormalities in brain development, with minimal changes in their superficial behavior and neurologic function. Additional studies of tissue and cultured cells from affected animals suggest a pathophysiologic mechanism in which increased death of neurons accompanied by increased cell division of astrocytes gives rise to abnormal organization of neuronal layers and loss of white matter. These results provide new insight into a developmental process that is unique to animals with gyrencephalic brains.

Introduction

Cerebral dysgenesis, or abnormal development of the telencephalon, encompasses a large number of malformations of cortical development including cortical dysplasia, microcephaly, heterotopia, schizencephaly, and polymicrogyria [1]. Clinical presentation of patients with cerebral dysgenesis can range from intellectual disability to severe epilepsy and neural tube defects [2]. Mendelian causes of cerebral dysgenesis in humans includes loss of function mutations in *WDR62*, *NDE1*, *DYNC1H1*, *KIF5C*, *KIF2A*, and *TUBG1* and related genes [3]. The vast majority of genes that regulate advanced cerebral cortical development have been discovered via forward genetic approaches in humans.

Gyrification refers to the process by which the cerebral cortex expands and folds. Overall size and gyrification of the cerebral cortex varies significantly between species [4], and increased cortical mass, cortical gyrification, and complex lamination within the cerebral cortex are traits that are associated with cognitive ability [5, 6]. Appropriate *in vivo* models of gyrification are limited as most laboratory animals exhibit minimal gyrification, and rodents (the most commonly used laboratory models) are lissencephalic [4]. However, the few studies that do exist in gyrencephalic models provide important insights into mechanisms of gyrification [7, 8], and gyrification studies are being conducted in relevant gyrencephalic species such as cats, sheep, and dogs [4]. Cats have prominent gyrification and are commonly used as a model for numerous neurologic diseases [9, 10].

Here we report that a loss of function mutation in *PEA15* (FelCat9 Chr. F1, 66768323 GT -> G) is likely responsible for a form of cerebral dysgenesis in the domestic cat, characterized by microcephaly and polymicrogyria. Characterization of the pathophysiological and neurodevelopmental consequences of *PEA15* deficiency offers insight into its essential role in gyrification and cortical development.

Results

Cerebral dysgenesis underlies an inherited neurodevelopmental abnormality in cats

An autosomal recessive, neurodevelopmental abnormality spontaneously arose in a domestic cat research colony at Auburn University. The mutation originated during outbreeding of cats used to study two lysosomal storage diseases, in which mutations were segregating for GM2 gangliosidosis variant AB (*GM2A*) [11], and mucopolysaccharidosis VI (*MPSVI*) [12]. The cerebral dysgenesis phenotype segregated independently from both of the known mutations in the colony (Table S1) and is clinically distinct from the lysosomal storage disease phenotypes, which lead to a progressive neurologic degeneration that is typically fatal prior to one year of age. Evaluation of 123 cats from the two breeding colonies identified 25 cats that were phenotypically affected with cerebral dysgenesis (S1 Figure). Of these affected cats, six were heterozygous, and three were homozygous for the *MPSVI* mutant allele, while one was heterozygous and three were homozygous for the *GM2A* mutant allele. None of the cats with cerebral dysgenesis were doubly homozygous for *MPSVI* and *GM2A* mutant alleles, and expressivity of the cerebral dysgenesis phenotype was not affected by carrier status of either *MPSVI* or *GM2A*.

Animals with cerebral dysgenesis exhibit spastic tetraparesis and ataxia first apparent around 3–4 weeks of age as they begin to walk. As the animals grow, spasticity and ataxia partially resolve, stabilizing by 6–9 months of age. At approximately 1.5 years, affected cats develop sensory abnormalities and often become aggressive. Sensory abnormalities manifest as stargazing and fly-biting: staring into empty space, and attacking or biting with no stimulus present, respectively. Aggressive behaviors were often erratic, unpredictable and included unprovoked attacks on long-term cage mates and caretakers. Some affected animals had seizures, although abnormal baseline EEG tracings were not observed. There were no deviations from reference intervals in complete blood count, serum biochemistry or urinalysis of affected cats, indicating that apart from the severe neurologic changes there was no additional systemic disease. Cerebrospinal fluid in carriers and affected cats showed no abnormalities or evidence of central nervous system inflammation (Table S2). In addition, cerebrospinal fluid enzyme activity

for markers of inflammation and neuronal cell damage were not significantly different from unaffected age-matched cats (S2 Figure). Taken together, these findings suggest that affected adult cats had a stable, non-progressive neurologic disease.

At necropsy, affected juvenile and adult cats exhibited generalized microcephaly and polymicrogyria with focal lissencephaly and regional gyral variability (Figure 1A - 1C). The most severely affected areas (frontoparietal) often had a cobblestone appearance. The average brain weight of affected cats was 4.3 grams per kilogram of body weight, while for unaffected and carrier cats average brain weight was 7.8 grams per kilogram, indicating a 45% decrease in brain mass (Figure 1D). In contrast to the significant abnormalities in the cerebral cortex, the size and structure of the cerebellum was normal with no vermal or hemispheric hypoplasia, dysplasia or agenesis.

Brains from affected cats aged 1–8 months were evaluated histologically in comparison to aged-matched controls (Figure 1E). Overall, affected cats exhibited variable thinning of the cerebral cortex, especially in dorsal and lateral regions, and disorganization of cortical layers. In severely affected areas, cortical neurons were present in an undulating laminar band reminiscent of gyri, but sulci were largely absent and gyral folds were irregular in size, location, distribution, and orientation. White matter of the corona radiata and internal capsule was markedly decreased in volume, but the corpus callosum was generally spared. Basal nuclei appeared normally organized, as did olfactory tubercles, olfaction tracts and thalamus, although all areas were smaller than age-matched controls. Recapitulating the impressions garnered at necropsy, the cerebellum was normally organized with all layers including an age-appropriate external granule layer in cats younger than 3–4 months.

Magnetic resonance imaging (MRI) showed similar gyrification abnormalities as observed grossly in necropsy samples with flattening of the parietal and temporal lobes (FIgure 2). Additionally, MRI suggested that decreased brain volume was due primarily to decreased white matter. The most dramatic changes noted on MRI were located at the perisylvian, ectosylvian and

cingulate gyri (Figure 2A – 2C), where there was serve attenuation of gyral formation and decreased white matter, particularly in the anterior region (Figure 2C).

PEA15 loss of function as the most likely Mendelian cause of cerebral dysgenesis.

To identify the underlying genetic cause of cerebral dysgenesis, we initially carried out whole genome sequencing (WGS) and RNA-seq-based genotyping of eight affected animals and six obligate carriers, applying zygosity-based filtering criteria under the model of complete penetrance of an autosomal recessive trait. We identified all variants that were homozygous in eight affected animals and heterozygous in the six obligate carriers, and observed a cluster of variants that was significantly enriched (p = 0.006, chi-square vs. random genome-wide distribution) in a 5 Mb region towards the end of chromosome F1 (Figure 3A).

To confirm and further fine-map the region, we carried out amplicon-based genotype-by-sequencing on an additional 91 cats (Figure 3, Table S1), using 26 variants across an ~70 Mb interval that contains the candidate region on chromosome F1, 4 additional variants that span the remainder of chromosome F1, and 20 variants from other chromosomes. All affected cats, but no unaffected cats, were homozygous for a 1.3 Mb haplotype on chromosome F1 (Figure 3B) in which the peak LOD score was 10.1 (Figure 3C, Table S3); all variants on chromosomes other than F1 exhibited LOD scores < 1.8 (Table S3).

Within the 1.3 Mb critical region, there are 2289 variants, of which 337 are not present in the 99 Lives dataset (an allele frequency database for cats described elsewhere [13]), including 4 in protein-coding sequence. Among all variants for which human orthology could be assigned, one, a single nucleotide deletion in *PEA15* (FelCat9 Chr. F1, 66768323 GT -> G), stood out as exhibiting the highest level of potential deleteriousness as assessed with combined annotation dependent depletion (CADD) (Figure 3D). The remaining 3 coding variants were either synonymous or not predicted to be damaging (Table 1), and lie in 2 genes that are not expressed

in brain (*ATP1A4*, 2 counts per million; *LY9*, 3 counts per million). By contrast, *PEA15* is highly expressed cat brain cortex by RNA-seq (401 counts per million) described further below.

In addition to considering single nucleotide and small indel variants, we surveyed the critical region for copy number and structural variants (Methods), and did not detect any changes consistent with the previously observed zygosity pattern. Furthermore, no assembly or coverage gaps were present in the 1.3 Mb candidate interval, and we found no evidence for structural variants based on discordant or clipped reads (Figure S3).

In cats and other species, including humans, *PEA15* encodes a 15 kDa protein of 130 amino acids that is highly conserved across species (Figure S4). The nucleotide deletion in *PEA15* lies towards the beginning of the second exon, and predicts a frameshift and truncated protein that lacks a critical ERK2 interaction domain (Figure 4A). Expression levels of *PEA15* as assessed by RNA-seq (described below) from the cerebral cortex of adult cats reveal a reduction of 59% in homozygous affected animals, consistent with nonsense-mediated decay (NMD) (Figure 4B). In further support of NMD, in cats that are heterozygous for the 1.3 Mb critical region, we observed a significant allele bias in *PEA15* compared to other genes in the critical region (Figure 4C). We examined protein levels by Western blot with a polyclonal antibody against C-terminal amino acids 93-123 of Human PEA15; a 15 kDa band apparent in normal brain extracts was absent in brains from affected animals (Figure 4D).

Neuropathology of cerebral dysgenesis.

MAP2 immunohistochemically (IHC) stained sections (Figure 5A) were assessed along with Luxol fast blue (LFB) histochemical stained sections (Figure 5B) to evaluate changes in grey matter thickness and overall white matter area. Affected cats had variably decreased cortical grey matter thickness compared to age-matched controls (Figure 5A), and marked reduction of the white matter that comprises the corona radiata and internal capsule (Figure 5B). Consistent with MRI

194 evaluation, there was an overall decrease in white matter which resulted in decreased area of
195 LFB staining (Figure 5C).

196 Cortical layering in affected cats was more disorganized and variable in layer thickness
197 compared to unaffected cats. Visually distinct cell populations like large pyramidal neurons were
198 present (Figure 6A). The molecular layer was more prominent in LFB and GFAP stained sections
199 owing to increased astrocyte density (Figure 6B). In unaffected cats, there were linear axonal
200 projections that were oriented perpendicularly to the cortical meningeal surface. In cats with
201 cerebral dysgenesis, perpendicular axonal orientation was reduced, with a denser and more
202 haphazard orientation of neuronal processes as compared to unaffected cats (Figure 6C).

203 We assessed the density of astrocytes, cells of oligodendrocytic origin, and microglia by
204 histomorphometry after immunostaining sections for GFAP, Olig-2, and IBA-1, respectively. The
205 only significant change in affected cats was an increase in staining density for GFAP, due to
206 increased numbers of grey matter astrocytes (Figure 7A-E). There was no significant difference
207 observed in Olig-2 staining (Figure 7F-J), however it should be noted that Olig-2 detects both
208 oligodendrocytic precursor cells, which can differentiate into neurons, astrocytes, and
209 oligodendrocytes, as well as mature myelinating oligodendrocytes. No difference was detected in
210 microglial density or morphology (Figure 7K-O).

211

212 *RNA-seq analysis*

213 To better understand the pathophysiologic mechanisms underlying cerebral dysgenesis, we
214 analyzed RNA-seq data from cerebral cortex of adult homozygous mutant (n=4), heterozygous
215 (n=3), and non-mutant (n=3) cats. 61 genes exhibited significant (FDR <0.05) differential
216 expression between homozygous mutant and non-mutant cats. Only 3 genes exhibited differential
217 expression between heterozygous mutant and non-mutant cats. Given minimal differences by
218 RNA-seq and that heterozygous mutant cats are unremarkable phenotypically, we also performed
219 a comparison of all 6 unaffected cats vs. homozygous mutant cats, revealing 25 differentially

expressed (FDR <0.05) genes. The intersection of genes that were differentially expressed in both the all unaffected vs. homozygous mutant comparison and non-mutant vs. homozygous mutant comparison results in a list of 16 differentially expressed genes (Figure 8A; Supplemental Table 4), including 5 upregulated collagen genes (*COL6A5*, *COL4A5*, *COL3A1*, *COL1A1*, and *COL6A1*; Figure 8B).

These observations, together with the neuropathologic observations that suggested profound abnormalities in cerebral development and cellular organization, suggested that gene expression changes in cortex might be utilized to assess changes in cellular composition. To explore this further, we analyzed the RNA-seq data with cell type-specific deconvolution analysis [14], in which genes are organized and plotted according to their differential expression, the extent of enrichment in a specific cell type, and the nominal significance of that observation. As depicted in Figure 9, many transcripts enriched in oligodendrocyte precursor cells are overrepresented (Figure 9A), while many transcripts enriched in mature oligodendrocytes are underrepresented (Figure 9B). Transcripts for mature astrocytes (Figure 9C) and endothelial cells (Figure 9D) also exhibited a slight but significant enrichment, while no differences were observed for neurons or microglia (Figure 9E, 9F). Overall, these results are consistent with the histomorphometery data, and suggest a pathologic mechanism in which axonal disorganization, failure of gyrification, and microcephaly are secondary to expansion of astrocytes and reduction of myelin-associated cells.

Effects of PEA15 deficiency on apoptosis and cell proliferation in cats.

Previous studies of *PEA15* in mice using a gene-targeted allele and a transgenic overexpression model demonstrated that it normally functions to suppress both TNFα-induced apoptosis [15] and cell proliferation during wound closure [16, 17]. We examined primary fibroblasts cultured from affected homozygous and non-mutant cats to investigate if those functions were conserved across species.

After treatment with TNFα, fibroblasts from affected animals exhibited reduced cell viability (Figure 9A) and increased caspase-8 activity (Figure 10B). Cell viability and caspase 8 activity did not change in the absence of TNFα treatment in fibroblasts from affected or unaffected animals. Exposure to FGFb for 72 hours yielded an ~ 2.5-fold increase in cell number in fibroblasts from unaffected animals, significantly elevated ($p = 0.02$) to ~3.5-fold in fibroblasts from affected animals (Figure 10C). Taken together, these results confirm that the effects of *PEA15* on apoptosis and cell proliferation are similar in cats and mice, and illustrate the functional impact of the *PEA15* mutation in cats with cerebral dysgenesis.

Discussion

PEA15 was originally described more than 25 years ago as a substrate for protein kinase C that is associated with microtubules and highly enriched in astrocytes [18]. Subsequent studies indicated that *PEA15* is expressed at low levels in almost all tissues [19] but exhibits increased expression in the brain, particularly during late gestation and the early postnatal period [20]. In mouse fibroblasts, PEA15 was characterized as an adapter protein that regulates proliferation through cytoplasmic interaction with ERK1/2 [21-23], and receptor-mediated apoptosis through interaction with the Fas-associated death domain (FADD) [18]. Many studies on PEA15 have focused on a potential role in insulin resistance due to its increased expression in fibroblasts, skeletal muscle, and adipose tissue during states of insulin resistance (reviewed elsewhere [24]). *Pea15* knockout mice exhibited normal brain size and morphology [15], but displayed mild spatial and temporal learning deficits attributed to the potential role of PEA15 as a mediator of ERK-dependent spatial learning [25].

The *PEA15* frameshift mutation we identified in domestic cats is associated with a loss of steady state mRNA and immunodetectable protein, and fibroblasts homozygous for the mutation exhibit abnormalities in response to TNFα and FGFb that recapitulate what has been described previously in mice and mouse cells. In contrast to mutant mice, however, in which

there are no obvious abnormalities in brain development, *PEA15* deficiency in cats is associated with extensive abnormalities in development and organization of the cerebral cortex that lead to a 45% decrease in overall brain weight, defective gyrification, expansion of astrocytes, and a loss of mature oligodendrocytes and white matter. Complete genomic sequence over the critical interval within which the cerebral dysgenesis mutation must lie identified no other plausible candidate variants except the *PEA15* frameshift mutation, and we conclude that *PEA15* deficiency is the likely cause of the neuropathologic abnormalities. Unlike many other domestic animals, application of gene editing technology to domestic cats faces a number of barriers and challenges, so it is not possible at present to further explore the pathogenicity of *PEA15* by generating new alleles, as might typically take place in laboratory mice. Nonetheless, there is a preponderance of evidence supporting a causal role for *PEA15* in cerebral dysgenesis, and we suggest that failure to observe a similar phenotype in mice has a simple explanation: the rodent brain is normally lissencephalic, and thus does not depend on extensive neuronal proliferation, expansion, and gyrification as it does in cats, dogs, and primates.

We propose a neuropathologic mechanism for the abnormalities described here whereby PEA15 normally serves to negatively regulate neuronal apoptosis and astrocyte proliferation (Figure 11, left), as has been demonstrated previously in mice. In the absence of PEA15, increased neuronal apoptosis and astrocyte proliferation leads to the production of excessive perineuronal nets, axonal disorganization and underdeveloped white matter tracts (Figure 11, right). Additional studies of *PEA15*-deficient cats should help determine at which phase of cortical development—neuroepithelial stem cell proliferation, neuronal stem cell migration, or synaptogenesis, apoptosis, and synaptic pruning—the postulated mechanisms are operative. We note, however, that the temporal pattern of *PEA15* expression, which peaks during late gestation and the early postnatal period, suggests a major role in the later stages of brain development, i.e. regulating neuronal apoptosis during synaptogenesis and synaptic pruning.

Although brain abnormalities in *PEA15*-deficient cats are striking, their gross appearance and behavior is not. Affected kittens were initially recognized due to a mild ataxia and were described by the husbandry staff as “shaky”; however, this gradually stabilized with age, and phenotype-based inference of disease status depends on an experienced clinician. Nonetheless, *PEA15* is under strong purifying selection—there is only a single amino acid substitution among mouse, cat, and human—and the gnomAD 2.1.1 [26] and TOPMed Bravo databases of human genome and exome data contains only 11 heterozygous loss-of-function variants (with none in the homozygous state) out of 198,527 non-overlapping individuals. Extrapolation suggests approximately five individuals on the planet with homozygous or compound heterozygous loss-of-function *PEA15* variants (assuming such a state would be consistent with life in humans), which may explain why it has not been previously recognized as a cause of human lissencephaly. In a recent summary of targeted sequencing studies for 17 genes in 811 patients with lissencephaly, a diagnostic rate of 81% was observed, in which > 99% of mutations were in *LIS1*, *DCX*, *TUBA1A*, or *DYNC1H1*, none of which are inherited in an autosomal recessive fashion.

In addition to identification of *PEA15* as a candidate gene for human lissencephaly, our work provides a new opportunity to investigate developmental mechanisms that underlie unique aspects of neurodevelopment in gyrencephalic species. Many of the processes disrupted by mutations in *LIS1*, *DCX, TUBA1A*, or *DYNC1H1* affect neuronal migration early in brain development, but, as noted above, the major role for *PEA15* in cortical development may occur later. As genomic tools for non-human animals continue to progress, careful clinical studies of companion and domestic animals are likely to lead to new insights into developmental and physiologic processes that are not present in conventional laboratory models.

Materials and Methods:

Study subjects and ethics statement

Animals included in this study are from the research colony at Auburn University College of Veterinary Medicine's Scott-Ritchey Research Center. Institutional Animal Care and Use Committee (IACUC) approval was obtained for all animal experiments. Animals evaluated in this study ranged in age from 1.2 months to 16 years and were evaluated in part based on videos that spanned a 20 year period. Based on breeding history, three adult cats within the colony were determined to be carriers. These cats along with three affected adults were also assessed by physical exam, including a complete neurological exam, serum biochemical analysis, complete blood count, MRI, and cerebrospinal fluid analysis. Cats were also evaluated for abnormalities associated with mutation in *GM2A* [11], and mucopolysaccharidosis VI (*MPSVI*) [12] which were independent of the phenotype observed here as described in the main text. Images of tissues depicted in Figures 1, 5, 6, and 7 are representative examples of a total of seven homozygous mutant and seven age-matched non-mutant animals that were examined by necropsy, and immunohistochemistry.

Whole genome sequencing and RNA-seq–based genotyping

Whole genome sequencing was carried out on five animals from a single nuclear family for whom there was comprehensive information available regarding phenotype and breeding history: two affected individuals, their obligate carrier parents, and an obligate carrier sibling (based on affected offspring), as indicated in Figure S1. For RNA-seq, we used tissue from two of the same animals used for WGS (a sibling pair—one affected, one obligate carrier), and 14 additional animals: six affected, four obligate carriers (based on pedigree information, Figure S1), and four unaffected and unrelated individuals with no known connection to the pedigree (Table S1).

Genomic DNA was isolated from liver samples using a Qiagen DNeasy Blood & Tissue kit according to the manufacturer's instructions. DNA sequencing libraries were prepared for sequencing on the Illumina HiSeq X by the HudsonAlpha Genomic Services Lab by Covaris shearing, end repair, adapter ligation, and PCR using standard protocols. Library concentrations

were normalized using KAPA qPCR prior to sequencing. After sequencing, adapters were trimmed and FastQ files were quality checked using Trim Galore! 0.4.0 (a wrapper for cutadapt 1.8.1 [27] and FastQC 0.10.1). Initially, trimmed reads were aligned using bwa 0.7.12 [28] to the Felis Catus 8.0 build. When it became available, reads were also aligned to the Felis Catus 9.0 build. Most analyses were conducted with the Felis Catus 8.0 build because chain files for liftover from the 99 lives database were not available initially; however, analyses of candidate genes were carried out with the 9.0 build since this assembly has no gaps over the critical linkage region. Aligned reads were sorted and duplicates were marked with Picard tools 1.131. GATK 3.5.0 [29] was used for indel realignment, base quality recalibration, gVCF generation, and joint genotyping of genomic DNA. For RNA-seq data (described further below), variants were called using VarScan 2.3.6 [30]. For the zygosity analysis depicted in Figure 3A, we required genotyping calls from at least 11/14 animals, to allow for contribution from regions with less coverage in some cats. snpEff 4.1 [31] was used for annotation and filtering, and PROVEAN 1.1.5 [32] was used for missense damage prediction. For the *PEA15* frameshift, genotypes were confirmed by Sanger sequencing in 25 affected or obligate carrier animals.

RNAseq and cell type deconvolution

Total RNA was extracted from the grey matter of the cerebral cortex of 16 cats (seven affected cats, five obligate carriers based on breeding records, Figure S1, Table S1, and four unaffected animals from a different pedigree that did not segregate the cerebral dysgenesis mutation) using the Qiagen RNeasy Lipid Tissue Mini Kit according to the manufacturer's instructions. Ages ranged from four months to six years for affected cats, 2–12 years for obligate carriers, and 2–5.5 years for unaffected cats. RNA was treated with TURBO DNase, and RIN scores were measured using a BioAnalyzer. Libraries were generated using polyA selection and an Illumina Nextera RNA-Seq protocol. Library concentrations were normalized using KAPA qPCR prior to sequencing. Libraries were sequenced with paired end 50 bp reads on an Illumina HiSeq 2500.

373 Data from RNAseq was processed using aRNApipe [33], a python wrapper for several tools.
374 Briefly, adapters were trimmed and FastQ files were quality checked using Trim Galore! 0.4.0 (a
375 wrapper for cutadapt 1.8.1 [27] and FastQC 0.10.1). Reads were aligned with STAR 2.4.2a [34]
376 to the Felis Catus 8.0 build and counted by gene with HTSeq 0.5.3 [35]. Count data were
377 normalized and analyzed using DESeq2 [36] in R.

378 We collected RNA-seq data from 16 cats (7 homozygous mutant, 5 heterozygous, and 4
379 homozygous non-mutant). For the homozygous mutant vs. non-mutant comparison depicted in
380 Figure 8A, 6 cats were excluded: 3 homozygous mutant kittens, 1 heterozygous mutant that died
381 from a generalized seizure, and 1 heterozygous mutant and 1 homozygous non-mutant that were
382 outliers on principal component analysis (Figure S5). 10 cats (4 homozygous mutant, 3
383 heterozygous mutant, and 3 homozygous non-mutant) remained for analysis. Transcripts were
384 considered for cell type deconvolution analysis if they were at least two fold enriched over any
385 other cell type with a raw p value of less than 0.2 using relative abundance described previously
386 [14].

387

388 *Amplicon sequencing*

389 Amplicon sequencing was conducted for 96 cats, 91 with no previous genotype information along
390 with one with genome sequencing and four with RNA-seq. Amplicons were chosen to span 26
391 variants spaced along the ~70 Mb interval that contained the candidate region on chromosome
392 F1 as determined by zygosity analysis (Figure 3A), 4 additional variants space along the
393 remainder of chromosome F1, and 20 variants from other chromosomes. Primers used are listed
394 in Table S5. After PCR with 1–2 primer pairs per reaction in 384-well plates, amplicons were
395 pooled for each cat and barcoded for sequencing by ligating adapters to A-tails. Library
396 concentrations were normalized using KAPA qPCR prior to sequencing. Amplicons were
397 sequenced using an Illumina MiSeq with 150 bp paired end reads. After sequencing, adapters
398 were trimmed and FastQ files were quality checked using Trim Galore! 0.4.0 (a wrapper for

399 cutadapt 1.8.1 [27] and FastQC 0.10.1). Trimmed reads were aligned using bwa 0.7.12 [28] to
400 the Felis Catus 8.0 build. Picard tools 1.131 was used to sort, mark duplicates, and index.
401 Platypus 0.8.1 [37] was used to call variants.
402
403 *Haplotyping, LOD Score Calculation, and Other Analysis & Statistics*
404 Merlin 1.1.2 [38] was used for haplotyping and LOD score calculation (Table S3), according to a
405 rare recessive model. Coverage was calculated using goleft indexcov 0.1.7 [39]. CNV analysis
406 was conducted with Delly 0.7.8 [40]. Other packages used for standard processing of VCFs were
407 vt [41], bcftools [42], and vcftools [43]. Liftover to hg38 for CADD [44] analysis was conducted
408 with Crossmap 0.2.7 [45]. PEA15 conservation was assessed using a previously published
409 sequence-to-structure-to-function workflow [46]. Other statistics were calculated in either R or
410 Prism 7.
411
412 *Histological and Immunohistochemical analysis*
413 Histological and immunohistochemical (IHC) analyses were performed on cats that ranged in age
414 from 1–8 months with age-matched controls. Luxol fast blue (LFB) staining was performed as
415 previously described [47] both with and without Cresyl-Echt violet counterstain.
416 Immunohistochemical stains were performed using Dako automated immunostainer (Autostainer
417 Link48, Dako-Agilent, Santa Clara, CA) using a low pH (6.1) antigen retrieval. IBA1 (Biocare
418 Medical, CP290A; 1:100 dilution) and Olig2 (Abcam, EPR2678; 1:200 dilution) antibodies were
419 incubated for 30 minutes. GFAP antibody (IR 52461-2 Dako-Agilent, Santa Clara, CA, no dilution)
420 was incubated for 20 minutes. MAP2 antibody (Sigma-Aldrich, HM-2; 1:1000 dilution) was
421 incubated for four hours. Detection was performed using the Dako EnVision HRP detection with
422 DAB chromogen and hematoxylin counterstain. For quantification, slides were digitally scanned
423 at 40x using an Aperio Scan Scope (Leica Biosystems, Buffalo Grove, IL, USA). Algorithms were
424 written to quantify stained area of DAB for each individual IHC stain or LFB stain using Visiopharm

quantitative digital histopathology software (Visiopharm, Hoersholm Denmark) and applied to all slides of an individual stain, except MAP2 as MAP2 had broad cytoplasmic staining that did not allow for individual cell density assessment.

Magnetic Resonance Imaging

MRI data were acquired as previously described on a seven Tesla MAGNETOM scanner (Siemens Healthcare, Erlangen, Germany) from adult affected (n=3), carrier (n=2) and unaffected (n=4) cats as previously described [48]. A 32-channel head coil (Nova Medical, Boston, Mass.) was used for all scans. Anatomical coronal images were acquired using 3D MPRAGE (Magnetization-PRepared RApid Gradient Echo) with 0.5mm isotropic resolution and TR/TE of 1910/2.5ms, followed by 2D axial T2 turbo spin echo (TSE) images with TR/TE of 5450/12ms and a resolution of (0.25x0.25x1) mm^3. MRI data were analyzed with EFilm 3.2 software (Merge Healthcare, Chicago).

Immunoblot analysis

Samples of feline cerebral cortex (5 – 10 mg) were homogenized in 400 µl of RIPA buffer (PIERCE, ThermoFisher, Waltham, MA, USA) with a hand-held micro-pestle for 30 sec, followed by passage through a 25G needle and kept on ice for 20 min. After centrifugation at 16,200 ×*g* for 30 min at 4˚C, the soluble fraction was transferred to a new tube and total protein concentration was determined by DC protein assay (Bio-Rad, Hercules, CA, USA). Following quantification, 33 µg of protein sample were mixed with 4× Laemmli sample buffer (Bio-Rad) containing 400mM Dithiothreitol. Protein fractions were separated with 18 % sodium dodecyl sulfate polyacrylamide gel electrophoresis, and transferred to Odyssey® nitrocellulose membrane (Li-Cor, Lincoln, NE, USA), blocked in LI-COR Odyssey blocking buffer (Lincoln, NE) for 1 h, and incubated with rabbit polyclonal anti-PEA-15 (C-terminal amino acids 93-123 of Human PEA15) antibody ab135694 (Abcam, Cambridge, UK) at a concentration of 1:100 and anti-GAPDH antibody (MAB374, EMD

Millipore, Burlington, MA, USA) at a concentration of 1:500. Secondary antibodies (1:15,000) were IRDye®680RD Goat anti-Rabbit IgG (H+L, Li-Cor) and IRDye®800CW Goat anti-Mouse IgG (H+L, Li-Cor), respectively. The fluorescent signal was detected using Odyssey® Infrared imaging system (Li-Cor).

Primary skin fibroblast culture

Primary fibroblasts were established from feline skin samples. Dulbecco's modified eagle's medium (DMEM, Corning, NY) supplemented with 10% fetal bovine serum (FBS), penicillin (100 IU/ml), streptomycin (100µg/ml), and amphotericin B (0.25 µg/ml) was used as a standard growth media. Briefly, collected skin pieces were placed with the connective tissue in direct contact with the culture surface and cultured in growth media for 5 to 7 days until visible colonies formed. After removing skin pieces, cells were further cultured in growth media or stored in liquid nitrogen in freezing media containing 10% dimethyl sulfoxide

Cell viability, caspase-8 activity, and cell proliferation assay

Cell viability and caspase-8 activity were assessed in order to determine the susceptibility of primary fibroblasts to TNF-α induced apoptosis. Colorimetric Cell Viability Kit I (WST-8 reagent, PromoKine, Heidelberg, Germany) and Caspase-Glo® 8 Assay (Promega, Madison, WI) were used for cell viability assay and caspase-8 assay, respectively. In brief, cells were seeded in 96-well multiwell tissue culture plates at a density of 15,000 cells/90 uL/well. After 20 hours of incubation at 37 ˚C, cells were treated with 10 ng/ml purified recombinant human TNF-α (Peprotech, Rocky Hill, NJ) prepared in growth media containing 10 µg/ml of Actinomycin D (MP Biomedicals, Solon, OH). Two identical plates were prepared for each experiment. Following 3 hours of TNF-α treatment, one plate was equilibrated to room temperature for 15 min, caspase-8 assay substrate was added and the luminescent signal was evaluated by Infinite M200 microplate reader (Tecan, Mannedorf, Switzerland) after 30 minutes of room temperature incubation. The

other plate was cultured for 6 hours post TNF-α treatment. WST-8 reagent was added to each well and the plate was incubated at 37 ˚C for 1.5 hours. Then, the absorbance at 450 nm was measured by Infinite M200 microplate reader. Cell proliferation was assessed in primary fibroblasts as percent response to fibroblast growth factor-b (FGFb) relative to untreated cells from each individual. Cells were seeded in 6-well multiwell tissue culture plates at a density of 90,000 cells/2 mL/well. After 20 hours of incubation at 37 ˚C, cells were treated with 20 ng/ml purified FGFb (Peprotech, Rocky Hill, NJ) prepared in growth media. Following 72 hours of FGFb treatment, cell were washed once with PBS(-) and dethatched with 0.25% trypsin-EDTA (Corning). The total cell number in each well was determined using trypan blue dye exclusion on a hemocytometer.

Data Availability

All sequencing data are publicly available at SRA Project PRJNA495843. Descriptors for each sample are included at SRA, and also in the supplemental table (S1 Table).

Acknowledgements

We thank Joseph Benito for technical assistance in generating RNA-seq libraries, Corneliu Henegar for assistance with computational scripts, Bandon Brunson for initial review of the histology, Edward Morrison for his review of the histopathology and guidance, Nancy Merner for her help with the pedigree, Matt Miller for reading and revising the manuscript, and Nancy Morrison for technical support in generating primary feline fibroblasts. 99 Lives Consortium members that contributed to the 99 Lives analysis used in this manuscript include: Reuben M. Buckley[1], Danielle Aberdein[2], Paulo C. Alves[3,4], Rebecca R. Bellone[5], Tomas F. Bergström[6], Adam R. Boyko[7], Jeffrey A. Brockman[8], Margret L. Casal[9], Marta G.

Castelhano[10], Ottmar Distl[11], Nicholas H. Dodman[12], N. Matthew Ellinwood[13], Jonathan E. Fogle[14], Oliver P. Forman[15], Dorian J. Garrick[2,13], Edward I. Ginns[16], Jens Häggström[17], Robert J. Harvey[18], Daisuke Hasegawa[19], Bianca Haase[20], Christopher R. Helps[21], Isabel Hernandez[22], Marjo K. Hytönen[23], Daniel M. Ibrahim[24-26], Maria Kaukonen[23], Tomoki Kosho[27], Emilie Leclerc[2,28], Teri L. Lear[29], Tosso Leeb[30], Ronald H.L. Li[31], Hannes Lohi[23], Maria Longeri[32], Dario G. Lupianez[33], Mark A. Magnuson[34], Richard Malik[35], Shrinivas Mane[36], John S. Munday[2], William J. Murphy[37], Niels C. Pedersen[38], Simon M. Peterson-Jones[39], Max F. Rothschild[13], Clare Rusbridge[40], Beth Shapiro[41], Joshua A. Stern[38], Orsolya Symmons[42], William F. Swanson[43], Karen A. Terio[44], Rory J. Todhunter[10], Wesley C. Warren[45], Elizabeth A. Wilcox[10], Julia H. Wildschutte[46], Yoshihiko Yu[19], and Leslie A. Lyons[1].

[1]Department of Veterinary Medicine and Surgery, College of Veterinary Medicine, University of Missouri, Columbia, Missouri, 65211 USA

[2]School of Veterinary Biomedical Science, Massey University, Palmerston North 4442 New Zealand

[3]CIBIO/InBIO, Centro de Investigação em Biodiversidade e Recursos Genéticos/InBIO Associate Lab & Faculdade de Ciências, Universidade do Porto, Campus e Vairão, 4485–661 Vila do Conde, Portugal

[4]Wildlife Biology Program, University of Montana, Missoula, Montana, 59812 USA

[5]Veterinary Genetics Laboratory, University of California, Davis, Davis California, 95616 USA

[6]Department of Animal Breeding and Genetics, Swedish University of Agricultural Sciences, 750 07 Uppsala, Sweden

[7]Department of Biomedical Sciences, College of Veterinary Medicine, Cornell University, Ithaca, New York, 14853 USA

[8]Hill's Pet Nutrition Inc., Topeka, Kansas 66601 USA

[9]Reproduction, and Pediatrics, School of Veterinary Medicine, University of Pennsylvania, Philadelphia, PA 19104 USA

[10]Department of Clinical Sciences, College of Veterinary Medicine, Cornell University, Ithaca, New York, 14853 USA

[11]Institute for Animal Breeding and Genetics, University of Veterinary Medicine Hannover (Foundation), 30559, Hannover, Germany

[12]Department of Clinical Sciences, Cummings School of Veterinary Medicine, Tufts University, Grafton, MA, 01536 USA

[13]Department of Animal Science, College of Agriculture and Life Sciences, Iowa State University, Ames, Iowa, 50011 USA

[14]College of Veterinary Medicine, North Carolina State University, Raleigh, NC 27607

[15]WALTHAM Centre for Pet Nutrition, Freeby Lane, Waltham on the Wolds, Leicestershire, LE14 4RT UK

[16]Department of Psychiatry, University of Massachusetts Medical School, Worcester, MA, 01655 USA

[17]Department of Clinical Sciences, Faculty of Veterinary Medicine and Animal Science, Swedish University of Agricultural Sciences, Uppsala, SE-750 07 Sweden

[18]School of Health and Sport Sciences, University of the Sunshine Coast, Sippy Downs, QLD, Australia

[19]Department of Clinical Veterinary Medicine, Nippon Veterinary and Life Science University, Tokyo 180-8602 Japan

[20]Sydney School of Veterinary Science, Faculty of Science, University of Sydney, Sydney, NSW, 2006, Australia

[21]Langford Vets, University of Bristol, Langford, Bristol, BS40 5DU UK

[22]Pediatrics and Medical Genetics Service, College of Veterinary Medicine, Cornell University, Ithaca, New York, 14853 USA

[23]Department of Veterinary Biosciences; Department of Medical Genetics, University of Helsinki and Folkhälsan Research Center, Helsinki 00014 Finland

[24]Max Planck Institute for Molecular Genetics, 14195 Berlin, Germany

[25]Institute for Medical and Human Genetics, Charité Universitätsmedizin Berlin, 13353 Berlin, Germany

[26]Berlin-Brandenburg Center for Regenerative Therapies, Charité-Universitätsmedizin Berlin, D 13353 Berlin, Germany.

[27]Department of Medical Genetics, Center for Medical Genetics, Shinshu University Hospital, Matsumoto, Nagano 390-8621, Japan

[28]SPF - Diana Pet food – Symrise Group – 56250 Elven, France

[29]Department of Veterinary Science, University of Kentucky - Lexington, Lexington, KY, 40506 USA (*In memoriam*)

[30]Vetsuisse Faculty, Institute of Genetics, University of Bern, 3001 Bern, Switzerland

[31]Department of Surgical and Radiological Sciences, School of Veterinary Medicine, University of California Davis, One Shields Ave, Davis, CA, 95616 USA

[32]Dipartimento di Medicina Veterinaria, University of Milan, 20122 Milan, Italy

[33]Epigenetics and Sex Development Group, Berlin Institute for Medical Systems Biology, Max-Delbrück Center for Molecular Medicine, Berlin-Buch, Germany.

[34]Departments of Molecular Physiology and Biophysics, Cell and Developmental Biology, and Medicine, Vanderbilt University, School of Medicine, Nashville, Tennessee, 37232 USA

[35]Centre for Veterinary Education, University of Sydney, Sydney, NSW, 2006 Australia

[36]Elanco Animal Health, Greenfield, IN 46140 USA

[37]Department of Veterinary Integrative Biosciences, College of Veterinary Medicine, Texas A&M University, College Station, Texas, 77845 USA

[38]Department of Medicine and Epidemiology, School of Veterinary Medicine, University of California at Davis, Davis, California, 95616 USA

[39]Small Animal Clinical Sciences, College of Veterinary Medicine, Michigan State University, East Lansing, Michigan, 48824 USA

[40]School of Veterinary Medicine, Faculty of Health & Medical Sciences, Univesity of Surrey, Guildford, Surrey, GU2 7AL, United Kingdom

[41]Department of Ecology and Evolutionary Biology, University of California, Santa Cruz, Santa Cruz, California 95064 USA

[42]Department of Bioengineering, University of Pennsylvania, Philadelphia, PA 19104, USA

[43]Center for Conservation and Research of Endangered Wildlife (CREW), Cincinnati Zoo & Botanical Garden, Cincinnati, Ohio, 45220 USA

[44]Zoological Pathology Program, University of Illinois, Brookfield, Illinois 60513 USA

592 [45]Division of Animal Sciences, College of Agriculture, Food and Natural Resources;

593 School of Medicine, University of Missouri, Columbia, Missouri 65211, USA

594 [46]Bowling Green State University, Department of Biological Sciences, Bowling Green,

595 Ohio 43403 USA

596 **References:**

597 1. Schaefer GB, Sheth RD, Bodensteiner JB. Cerebral dysgenesis. An overview.
598 Neurologic clinics. 1994;12(4):773–88. Epub 1994/11/01. PubMed PMID: 7845342.
599 2. Parrini E, Conti V, Dobyns WB, Guerrini R. Genetic Basis of Brain Malformations.
600 Molecular syndromology. 2016;7(4):220–33. Epub 2016/10/27. doi: 10.1159/000448639.
601 PubMed PMID: 27781032; PubMed Central PMCID: PMCPMC5073505.
602 3. Poirier K, Lebrun N, Broix L, Tian G, Saillour Y, Boscheron C, et al. Mutations in TUBG1,
603 DYNC1H1, KIF5C and KIF2A cause malformations of cortical development and microcephaly.
604 Nat Genet. 2013;45(6):639–47. Epub 2013/04/23. doi: 10.1038/ng.2613. PubMed PMID:
605 23603762; PubMed Central PMCID: PMCPMC3826256.
606 4. Defelipe J. The evolution of the brain, the human nature of cortical circuits, and
607 intellectual creativity. Front Neuroanat. 2011;5:29. Epub 2011/06/08. doi:
608 10.3389/fnana.2011.00029. PubMed PMID: 21647212; PubMed Central PMCID:
609 PMCPMC3098448.
610 5. Sun T, Hevner RF. Growth and folding of the mammalian cerebral cortex: from
611 molecules to malformations. Nat Rev Neurosci. 2014;15(4):217–32. Epub 2014/03/22. doi:
612 10.1038/nrn3707. PubMed PMID: 24646670; PubMed Central PMCID: PMCPMC4107216.
613 6. Gregory MD, Kippenhan JS, Dickinson D, Carrasco J, Mattay VS, Weinberger DR, et al.
614 Regional Variations in Brain Gyrification Are Associated with General Cognitive Ability in
615 Humans. Curr Biol. 2016;26(10):1301–5. Epub 2016/05/03. doi: 10.1016/j.cub.2016.03.021.
616 PubMed PMID: 27133866; PubMed Central PMCID: PMCPMC4879055.
617 7. Matsumoto N, Shinmyo Y, Ichikawa Y, Kawasaki H. Gyrification of the cerebral cortex
618 requires FGF signaling in the mammalian brain. Elife. 2017;6. Epub 2017/11/15. doi:
619 10.7554/eLife.29285. PubMed PMID: 29132503; PubMed Central PMCID: PMCPMC5685484.
620 8. Shinmyo Y, Terashita Y, Dinh Duong TA, Horiike T, Kawasumi M, Hosomichi K, et al.
621 Folding of the Cerebral Cortex Requires Cdk5 in Upper-Layer Neurons in Gyrencephalic

622 Mammals. Cell Rep. 2017;20(9):2131–43. Epub 2017/08/31. doi: 10.1016/j.celrep.2017.08.024.
623 PubMed PMID: 28854363.
624 9. Griffin BBHJ. Domestic Cats as Laboratory Animal Models. 2nd ed. Fox JG, editor:
625 Academic Press; 2002. 22 p.
626 10. Gurda BL, Bradbury AM, Vite CH. Canine and Feline Models of Human Genetic
627 Diseases and Their Contributions to Advancing Clinical Therapies. Yale J Biol Med.
628 2017;90(3):417–31. Epub 2017/09/29. PubMed PMID: 28955181; PubMed Central PMCID:
629 PMCPMC5612185.
630 11. Martin DR, Cox NR, Morrison NE, Kennamer DM, Peck SL, Dodson AN, et al. Mutation
631 of the GM2 activator protein in a feline model of GM2 gangliosidosis. Acta Neuropathol.
632 2005;110(5):443–50. Epub 2005/10/04. doi: 10.1007/s00401-005-1040-6. PubMed PMID:
633 16200419.
634 12. Jezyk PF, Haskins ME, Patterson DF, Mellman WJ, Greenstein M.
635 Mucopolysaccharidosis in a cat with arylsulfatase B deficiency: a model of Maroteaux-Lamy
636 syndrome. Science. 1977;198(4319):834–6. Epub 1977/11/25. doi: 10.1126/science.144321.
637 PubMed PMID: 144321.
638 13. Lyons LA, Creighton EK, Alhaddad H, Beale HC, Grahn RA, Rah H, et al. Whole
639 genome sequencing in cats, identifies new models for blindness in AIPL1 and somite
640 segmentation in HES7. BMC Genomics. 2016;17:265. Epub 2016/04/01. doi: 10.1186/s12864-
641 016-2595-4. PubMed PMID: 27030474; PubMed Central PMCID: PMCPMC4815086.
642 14. Zhang Y, Chen K, Sloan SA, Bennett ML, Scholze AR, O'Keeffe S, et al. An RNA-
643 sequencing transcriptome and splicing database of glia, neurons, and vascular cells of the
644 cerebral cortex. J Neurosci. 2014;34(36):11929–47. doi: 10.1523/JNEUROSCI.1860-14.2014.
645 PubMed PMID: 25186741; PubMed Central PMCID: PMCPMC4152602.
646 15. Kitsberg D, Formstecher E, Fauquet M, Kubes M, Cordier J, Canton B, et al. Knock-out
647 of the neural death effector domain protein PEA-15 demonstrates that its expression protects

astrocytes from TNFalpha-induced apoptosis. J Neurosci. 1999;19(19):8244–51. Epub 1999/09/24. PubMed PMID: 10493725.

16. Ascione F, Vasaturo A, Caserta S, D'Esposito V, Formisano P, Guido S. Comparison between fibroblast wound healing and cell random migration assays in vitro. Experimental cell research. 2016;347(1):123–32. Epub 2016/08/01. doi: 10.1016/j.yexcr.2016.07.015. PubMed PMID: 27475838.

17. Buonomo R, Giacco F, Vasaturo A, Caserta S, Guido S, Pagliara V, et al. PED/PEA-15 controls fibroblast motility and wound closure by ERK1/2-dependent mechanisms. J Cell Physiol. 2012;227(5):2106–16. Epub 2011/07/23. doi: 10.1002/jcp.22944. PubMed PMID: 21780113; PubMed Central PMCID: PMCPMC3306794.

18. Renault F, Formstecher E, Callebaut I, Junier MP, Chneiweiss H. The multifunctional protein PEA-15 is involved in the control of apoptosis and cell cycle in astrocytes. Biochem Pharmacol. 2003;66(8):1581–8. Epub 2003/10/14. PubMed PMID: 14555237.

19. Estelles A, Yokoyama M, Nothias F, Vincent JD, Glowinski J, Vernier P, et al. The major astrocytic phosphoprotein PEA-15 is encoded by two mRNAs conserved on their full length in mouse and human. J Biol Chem. 1996;271(25):14800–6. Epub 1996/06/21. PubMed PMID: 8662970.

20. Danziger N, Yokoyama M, Jay T, Cordier J, Glowinski J, Chneiweiss H. Cellular expression, developmental regulation, and phylogenic conservation of PEA-15, the astrocytic major phosphoprotein and protein kinase C substrate. J Neurochem. 1995;64(3):1016–25. Epub 1995/03/01. PubMed PMID: 7861130.

21. Formisano P, Ragno P, Pesapane A, Alfano D, Alberobello AT, Rea VE, et al. PED/PEA-15 interacts with the 67 kD laminin receptor and regulates cell adhesion, migration, proliferation and apoptosis. J Cell Mol Med. 2012;16(7):1435–46. Epub 2011/09/08. doi: 10.1111/j.1582-4934.2011.01411.x. PubMed PMID: 21895963; PubMed Central PMCID: PMCPMC3823213.

674 22. Mace PD, Wallez Y, Egger MF, Dobaczewska MK, Robinson H, Pasquale EB, et al.
675 Structure of ERK2 bound to PEA-15 reveals a mechanism for rapid release of activated MAPK.
676 Nat Commun. 2013;4:1681. Epub 2013/04/12. doi: 10.1038/ncomms2687. PubMed PMID:
677 23575685; PubMed Central PMCID: PMCPMC3640864.
678 23. Exler RE, Guo X, Chan D, Livne-Bar I, Vicic N, Flanagan JG, et al. Biomechanical insult
679 switches PEA-15 activity to uncouple its anti-apoptotic function and promote erk mediated tissue
680 remodeling. Experimental cell research. 2016;340(2):283–94. Epub 2015/12/01. doi:
681 10.1016/j.yexcr.2015.11.023. PubMed PMID: 26615958.
682 24. Fiory F, Spinelli R, Raciti GA, Parrillo L, D'Esposito V, Formisano P, et al. Targetting
683 PED/PEA-15 for diabetes treatment. Expert Opin Ther Targets. 2017;21(6):571–81. Epub
684 2017/04/12. doi: 10.1080/14728222.2017.1317749. PubMed PMID: 28395542.
685 25. Ramos JW, Townsend DA, Piarulli D, Kolata S, Light K, Hale G, et al. Deletion of PEA-
686 15 in mice is associated with specific impairments of spatial learning abilities. BMC
687 neuroscience. 2009;10:134. Epub 2009/11/18. doi: 10.1186/1471-2202-10-134. PubMed PMID:
688 19917132; PubMed Central PMCID: PMCPMC2781817.
689 26. Lek M, Karczewski KJ, Minikel EV, Samocha KE, Banks E, Fennell T, et al. Analysis of
690 protein-coding genetic variation in 60,706 humans. Nature. 2016;536(7616):285–91. doi:
691 10.1038/nature19057. PubMed PMID: 27535533; PubMed Central PMCID: PMCPMC5018207.
692 27. Martin M. Cutadapt removes adapter sequences from high-throughput sequencing
693 reads. EMBnet journal. 2011;17(1):pp. 10–2.
694 28. Li H, Durbin R. Fast and accurate short read alignment with Burrows–Wheeler
695 transform. Bioinformatics. 2009;25(14):1754–60.
696 29. McKenna A, Hanna M, Banks E, Sivachenko A, Cibulskis K, Kernytsky A, et al. The
697 Genome Analysis Toolkit: a MapReduce framework for analyzing next-generation DNA
698 sequencing data. Genome res. 2010;20(9):1297–303.

30. Koboldt DC, Zhang Q, Larson DE, Shen D, McLellan MD, Lin L, et al. VarScan 2: somatic mutation and copy number alteration discovery in cancer by exome sequencing. Genome res. 2012;22(3):568–76.

31. Cingolani P, Platts A, Wang LL, Coon M, Nguyen T, Wang L, et al. A program for annotating and predicting the effects of single nucleotide polymorphisms, SnpEff: SNPs in the genome of Drosophila melanogaster strain w1118; iso-2; iso-3. Fly. 2012;6(2):80–92.

32. Choi Y, Chan AP. PROVEAN web server: a tool to predict the functional effect of amino acid substitutions and indels. Bioinformatics. 2015;31(16):2745–7.

33. Alonso A, Lasseigne BN, Williams K, Nielsen J, Ramaker RC, Hardigan AA, et al. aRNApipe: a balanced, efficient and distributed pipeline for processing RNA-seq data in high-performance computing environments. Bioinformatics. 2017;33(11):1727–9.

34. Dobin A, Davis CA, Schlesinger F, Drenkow J, Zaleski C, Jha S, et al. STAR: ultrafast universal RNA-seq aligner. Bioinformatics. 2013;29(1):15–21.

35. Anders S, Pyl PT, Huber W. HTSeq—a Python framework to work with high-throughput sequencing data. Bioinformatics. 2015;31(2):166–9.

36. Love MI, Huber W, Anders S. Moderated estimation of fold change and dispersion for RNA-seq data with DESeq2. Genome Biol. 2014;15(12):550.

37. Rimmer A, Phan H, Mathieson I, Iqbal Z, Twigg SR, Wilkie AO, et al. Integrating mapping-, assembly-and haplotype-based approaches for calling variants in clinical sequencing applications. Nat Genet. 2014;46(8):912.

38. Abecasis GR, Cherny SS, Cookson WO, Cardon LR. Merlin—rapid analysis of dense genetic maps using sparse gene flow trees. Nat Genet. 2002;30(1):97.

39. Pedersen BS, Collins RL, Talkowski ME, Quinlan AR. Indexcov: fast coverage quality control for whole-genome sequencing. GigaScience. 2017.

723 40. Rausch T, Zichner T, Schlattl A, Stütz AM, Benes V, Korbel JO. DELLY: structural
724 variant discovery by integrated paired-end and split-read analysis. Bioinformatics.
725 2012;28(18):i333–i9.
726 41. Tan A, Abecasis GR, Kang HM. Unified representation of genetic variants.
727 Bioinformatics. 2015;31(13):2202–4. Epub 2015/02/24. doi: 10.1093/bioinformatics/btv112.
728 PubMed PMID: 25701572; PubMed Central PMCID: PMCPMC4481842.
729 42. Li H, Handsaker B, Wysoker A, Fennell T, Ruan J, Homer N, et al. The sequence
730 alignment/map format and SAMtools. Bioinformatics. 2009;25(16):2078–9.
731 43. Danecek P, Auton A, Abecasis G, Albers CA, Banks E, DePristo MA, et al. The variant
732 call format and VCFtools. Bioinformatics. 2011;27(15):2156–8.
733 44. Kircher M, Witten DM, Jain P, O'Roak BJ, Cooper GM, Shendure J. A general
734 framework for estimating the relative pathogenicity of human genetic variants. Nat Genet.
735 2014;46(3):310–5. doi: 10.1038/ng.2892. PubMed PMID: 24487276; PubMed Central PMCID:
736 PMCPMC3992975.
737 45. Zhao H, Sun Z, Wang J, Huang H, Kocher J-P, Wang L. CrossMap: a versatile tool for
738 coordinate conversion between genome assemblies. Bioinformatics. 2013;30(7):1006–7.
739 46. Prokop JW, Lazar J, Crapitto G, Smith DC, Worthey EA, Jacob HJ. Molecular modeling
740 in the age of clinical genomics, the enterprise of the next generation. J Mol Model.
741 2017;23(3):75. Epub 2017/02/17. doi: 10.1007/s00894-017-3258-3. PubMed PMID: 28204942;
742 PubMed Central PMCID: PMCPMC5529140.
743 47. Luna LG. Manual of Histologic Staining Methods of the Armed Forces Institute of
744 Pathology.: Blakiston Division, McGraw-Hill; 1968.
745 48. Gray-Edwards HL, Regier DS, Shirley JL, Randle AN, Salibi N, Thomas SE, et al. Novel
746 Biomarkers of Human GM1 Gangliosidosis Reflect the Clinical Efficacy of Gene Therapy in a
747 Feline Model. Molecular therapy : the journal of the American Society of Gene Therapy.

748 2017;25(4):892–903. Epub 2017/02/27. doi: 10.1016/j.ymthe.2017.01.009. PubMed PMID:

749 28236574; PubMed Central PMCID: PMCPMC5383552.

750

751

752

753 **Table 1: Variants in coding sequence in the linkage region not present in the 99**
754 **Lives dataset.** Note that two of the variants are synonymous in genes not expressed in
755 brain. Of the two variants that change coding sequence, the missense variant in *LY9* is
756 not predicted to be damaging, and *LY9* is not expressed in brain. In contrast, the
757 frameshift variant in *PEA15* is predicted to be highly damaging, and *PEA15* is
758 expressed a high level in brain.
759
760
761
762

Gene	Transcript	HGVS DNA	HGVS Protein	Protein Change	CADD	GERP	Cat Brain CPM	Human Brain CPM
LY9	XM_019822310.1	c.654A>G	p.Pro218Pro	Synonymous	0.0	-5.0	2.4	0.2
LY9	XM_019822310.1	c.478A>G	p.Met160Val	Missense	0.0	-7.9	2.4	0.2
PEA15	XM_023247767.1	c.176delA	p.Asn59fs	Frameshift	29.7	5.5	400.8	1087
ATP1A4	XM_023247847.1	c.1818C>T	p.Ala606Ala	Synonymous	NA (Hum. Ref.=A)		3.1	0.1

Figure Legends

Figure 1. Affected cats have marked microcephaly with polymicrogyria. Images of whole brain from (**A**) adult unaffected (+/+), and (**B**) adult and (**C**) juvenile affected (-/-) cats. Affected cats have dramatically decreased cerebral cortex size with normal formation of the cerebellum. (**D**) Brain weights of affected cats are significantly decreased with or without normalization to body weight, which is similar to unaffected cats. (**E**) Representative sections (left image, normal; right image, affected) from the region of the parietal cortex have gyrification defects characterized by shallow sulci and fusion of small gyri consistent with polymicrogyria, as well as abnormal white matter of the corona radiata and internal capsule.

Figure 2. Changes in MRI are consistent with microcephaly and attenuation of gyral formation. (**A**) Selected images from the frontoparietal region demonstrate marked attenuation and loss of gyral formation and white matter. Note the blurring of gray and white matter boundaries, especially apparent in the corona radiata. (**B**) Magnified region within the white box highlights the severe attenuation of the (**C**) anterior cingulate gyrus, outlined in white.

Figure 3. Zygosity mapping, linkage, and haplotype analysis identifies a frameshift in *PEA15* as the cause of cerebral dysgenesis. (**A**) Zygosity mapping, identifying all variants that are homozygous in 8 affected animals and heterozygous in 6 obligate carriers. Variants cluster in a region on the distal end of chromosome F1. (**B**) Diplotypes of 49 cats according to disease status as indicated. 13 diplotypes were imputed from progeny: the top 4 diplotypes are founders (note uncertain haplotype, denoted by X's), the next 5 diplotypes are for the next generation after the founders, and 4 other cats throughout the pedigree were imputed because a sample was not available. In the unaffected genotyped block, the cat indicated with a › is a cat that has 2 normal diplotypes but is present in the analysis because it was bred with a cat homozygous for the

788 disease diplotype. All affected animals are homozygous for a 1.3 Mb region (dashed black lines)
789 (**C**) Linkage analysis confirms that the 1.3 Mb region on chromosome F1 identified by zygosity
790 and haplotype analysis cosegregates with cerebral dysgenesis (coordinates given according to
791 Felcat8). (**D**) CADD scores for all variants in the 1.3 Mb critical region that are homozygous in
792 affected cats and absent from the 99 Lives dataset. Only 4 coding variants are present (see detail
793 in **Table 1**). The 2 variants in *LY9* (not expressed in brain) are overlapping in the lower left corner.
794 The 1 synonymous coding variant in *ATP1A4* (not expressed in brain) does not have a CADD
795 score because the alternate allele is reference in human and therefore is not plotted here. The
796 final coding variant in the region is a frameshift in *PEA15*, which is highly expressed in brain. The
797 variant is predicted to be highly damaging by CADD.
798
799
800 **Figure 4. The *PEA15* mutation introduces a premature termination codon, and PEA15**
801 **protein is absent in affected cats.** (**A**) Map of *PEA15* demonstrating the mutation location near
802 the beginning of Exon 2. (**B**) Overall levels of *PEA15* transcripts measured by RNA-Seq are
803 decreased in cats homozygous for the *PEA15* mutation (One-way ANOVA *p<0.0001, *p<0.01
804 by Tukey's *post hoc*). (**C**) Reads from the mutant *PEA15* allele in heterozygous cats are
805 significantly reduced compared to non-mutant reads, while heterozygous variants in nearby genes
806 do not exhibit allele bias (One-way ANOVA *p<0.0001, *p<0.001 by Tukey's *post hoc* vs. all of 3
807 nearby genes comparing the % variant reads per cat as the unit of comparison with 24 to >3,000
808 reads contributing to each % measurement for each gene). (**D**) PEA15 is absent from affected
809 animals by western blot.
810
811 **Figure 5. Affected cats have a significant loss of white matter.** (**A**) Subgross sections of
812 MAP2 stained neurons highlight the variable decrease in cortical thickness, and the reduced

area of the corona radiata (arrows) and internal capsule. (**B**) Subgross sections of Luxol fast blue (LFB) stained for myelin indicates decreased white matter, (**C**) which is confirmed through quantification of LFB stained sections of the frontopareital region.

Figure 6. Affected cats have loss of normal cerebral cortical layering, increased grey matter astrocytosis, and abnormal neuronal and axonal orientation. (**A**) Photomicrographs of Luxol fast blue – Cresyl Echt Violet (LFB-CEV) stained sections depicting vertical columns in the parietal region of unaffected (left) and age-matched affected (right) cats. In unaffected cats, 6 cortical layers extend from below the meninges (beginning with layer I, molecular layer) to the white matter (WM). In affected cats, grey matter thickness and column morphology are altered with disorganized layering. (**B**) Photomicrographs of GFAP stained sections of vertical columns reveals that affected cats exhibit a relative astrocytosis. Dotted lines indicate separation of white matter and grey matter. (**C**) Photomicrographs from MAP2 stained sections taken at approximately layers IV and V. Unaffected cats have linear axonal projections oriented perpendicular to the cortical meningeal surface while affected cats lack axonal directionality (bar = 20uM). In all images, the meningeal edge is located at the top.

Figure 7. Affected cats have significantly increased astrocyte density within the grey matter. (**A-B**) GFAP immunohistochemistry (IHC) of grey matter indicates increased density of astrocytes. (**C-E**) Digital image-analysis algorithms measured a significant increase in GFAP stain density primarily in grey matter stain. (**F-J**) Olig-2 staining indicates no significant change in the density of oligodendrocytes in grey matter, though an insignificant decrease of ~30% was noted in white matter. (**K-L**) No significant change in the density or morphology of microglia was detected in affected cats. (**M-O**) Microglial density findings are confirmed on quantification of IBA-1 stain. (bar = 200um)

839 **Figure 8. Differential expression analysis.** (**A**) Log2-fold change vs. magnitude of gene
840 expression for homozygous mutant (M–mutant) (n=4) vs all unaffected (N&C–normal and
841 carrier) (n=6) (heterozygous mutant (C–carrier) (n=3) and homozygous non-mutant (N–normal)
842 (n=3)). Genes with a significant difference for the strict criteria of significance in both
843 homozygous mutant (n=4) vs all unaffected (n=6) and homozygous mutant (n=4) vs
844 homozygous non-mutant (n=3) are labeled (triangles). Data was collected for an additional 6
845 animals, but excluded because of age, cause of death, or principal component analysis results
846 (**Methods**; **Table S4**; **Figure S5**). (**B**) Quantitative changes in collagen gene expression for
847 homozygous mutant, heterozygous, and homozygous non-mutant animals. No differences
848 (p=0.61, two-way ANOVA) were detected between normal and carrier cats.
849
850 **Figure 9. Differences in levels of cell type–specific transcripts suggest altered cellular**
851 **composition in the brains of affected cats.** (**A**) Oligodendrocyte precursor cell–specific
852 transcripts are increased in affected cats (Two-way ANOVA *p<0.0001 genotype effect). (**B**)
853 Oligodendrocyte–specific transcripts are decreased in affected cats (Two-way ANOVA *p<0.0001
854 genotype effect). (**C**) Astrocyte–specific transcripts are increased in affected cats (Two-way
855 ANOVA *p<0.0001 genotype effect). (**D**) Endothelial cell–specific transcripts are increased in
856 affected cats (Two-way ANOVA *p<0.0001 genotype effect). (**E**) Neuron–specific transcripts did
857 not change significantly (Two-way ANOVA p=0.60 genotype effect). (**F**) Microglia–specific
858 transcripts did not change significantly (Two-way ANOVA p=0.52 genotype effect).
859
860 **Figure 10. Differences in cytokine-mediated apoptosis and proliferation in affected**
861 **fibroblasts.** When treated with TNFα, there is (**A**) a significant decrease in cell viability and (**B**)
862 a significant increase in caspase-8 activity of primary dermal fibroblasts from affected cats
863 compared to unaffected cats. (**C**) When treated with 20ng/mL FGFb, proliferation is significantly

increased in primary dermal fibroblasts from affected cats compared to unaffected cats. There was no significant difference of untreated cells for either genotype.

Figure 11. Hypothesized mechanisms of PEA15 mediated cerebral dysgenesis in domestic cats. Beginning in late gestation through the early post-natal period of normal animals, there is increased neuronal apoptosis during synaptic pruning. PEA15, which is normally expressed at this time in the brain, protects from excessive apoptosis of neurons and inhibits proliferation of stimulated astrocytes. Therefore, loss of PEA15 is expected to cause increased neuronal apoptosis and increased proliferation of astrocytes. Grey matter astrocytosis may be a direct response to the increased apoptosis or neurons (reactive astrocytosis), and/or and excessive proliferation due to loss of PEA15 function. Abundant astrocytes produce excessive extracellular matrix which can form perineuronal nets and cause a premature end of the critical period for synaptic plasticity. These changes in development result in disorganized axonal development and underdeveloped white matter tracts which manifest as cerebral dysgenesis.

Supporting Information

S1 Table. Table of cats from the GM2A and MPSVI breeding colonies where the cerebral dysgenesis mutation was identified. Affected status is denoted by color with unaffected in white, obligate carriers based on breeding in grey, and affected cats in black.

S2 Table. Cerebrospinal Fluid Analysis. Cerebrospinal fluid protein concentration and cell counts in affected and carrier cats with a reference interval based on normal cats that was established by the Auburn University small animal teaching hospital.

S3 Table. Haplotyping and LOD Score Calculation. Merlin 1.1.2 was used for haplotyping and LOD score calculation. LOD score was calculated using parametric linkage analysis assuming a rare recessive model. Each marker is considered independently, equivalent to a theta value of zero. Note that, while we focused genotyping on chromosome F1 based on homozygosity mapping, we selectively genotyped a handful of markers on other chromosomes.

S4 Table. RNA-seq counts and differentially expressed genes. See excel file. Summary statistics are listed for each gene, and counts per million are listed for each cat, with exclusion criteria for cats not included in summary statistics noted.

S5 Table. Primer pairs for amplicon sequencing. Note that multiple primer pairs were included for the top nominated region to maximize genotyping success and increase coverage. The *PEA15* frameshift site is bolded.

S1 Fig. Pedigree. Phenotype is denoted by color and indicated on the pedigree with unaffected in white, obligate carriers with a central dot, and homozygous mutant cats in black.

S2 Fig. Cerebrospinal fluid enzyme activity. (**A**) Changes in aspartate amino transferase and (**B**) lactate dehydrogenase enzyme activity in adult cats (n = 3) from the cerebral dysgenesis cohort.

913 **S3 Fig. FelCat9 coverage.** (**A**) When averaged over 10,000 base pair windows, coverage stays
914 above 30x for all cats across the window linked to the phenotype. (**B**) When averaged over 1,000
915 base pair windows, only a few regions dip below 20x coverage. (**C**) Regions with less than 20x
916 coverage in all 5 cats. Note that regions are either in repetitive intronic or intergenic regions.
917
918 **S4 Fig. PEA15 Conservation.** (**A**) Conservation of PEA15 gene sequence was performed
919 using the open reading frames from 150 species. Scores at each codon were assessed, where
920 100% conservation corresponds to a score of 1, and this score also receives the addition of 0 if
921 dN-dS of the site is below the mean, addition of 0.25 for sites with values above the mean to 1
922 standard deviation above the mean, addition of 0.5 for sites greater than 1 standard deviation
923 but below 2 standard deviations, and addition of 1 for sites greater than 2 standard deviations.
924 Therefore, a score of 2 is maximal suggesting an amino acid that is 100% conserved with codon
925 wobble indicative of a high selection rate at the position. (**B**) Conservation values were placed
926 on a 21-codon sliding window (combining values for 10 codons before and after each position)
927 to identify conserved motifs within the gene. (**C**) Model of PEA15 protein with a structural z-
928 score of 0.12 (assessed with YASARA2 knowledge-based force field) suggesting accurate
929 predictions of fold space. Colors are based on 150 species alignments fed into ConSurf.
930
931 **S5 Fig. Principal component analysis (PCA) of RNA-seq data from cat cortex.** Out of 16
932 original cats, 1 cat was excluded from further analysis because of death by grand mal seizure,
933 evident by PCA. 3 cats were excluded from further analysis because they were kittens to avoid
934 detection of developmental false positive signals in differential expression analysis (1 kitten was
935 also an outlier by PCA). 2 cats were excluded on the basis of being clear outliers by PCA. 10
936 cats (4 homozygous mutant, 3 heterozygous mutant, and 3 homozygous non-mutant) remained
937 for analysis.

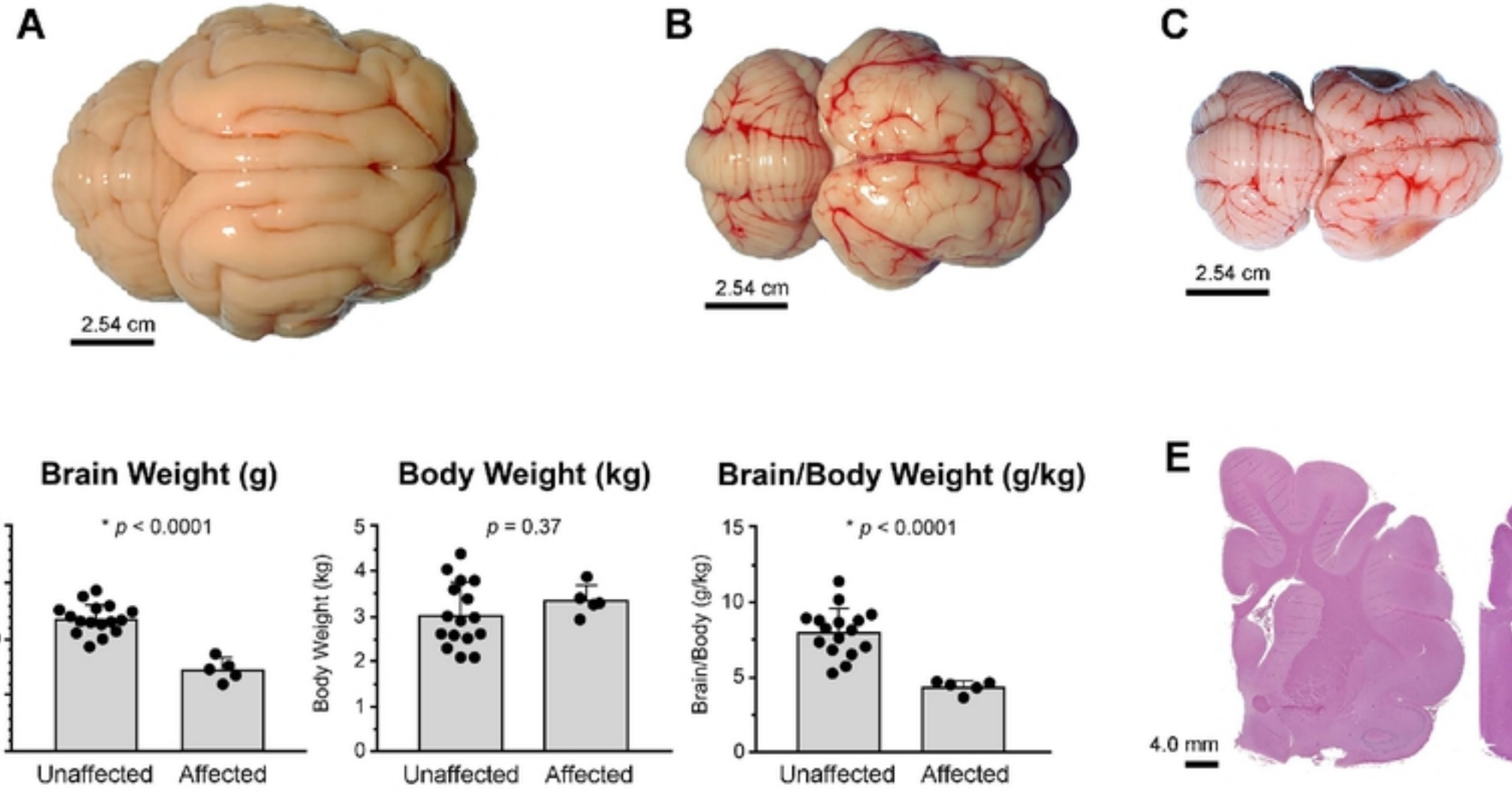
A
2.54 cm
B
2.54 cm
C
2.54 cm
D
Brain Weight (g)
* p < 0.0001
Brain Weight (g)
40
30
20
10
0
Unaffected
Affected
Body Weight (kg)
p = 0.37
Body Weight (kg)
5
4
3
2
1
0
Unaffected
Affected
Brain/Body Weight (g/kg)
* p < 0.0001
Brain/Body (g/kg)
15
10
5
0
Unaffected
Affected
E
4.0 mm

Unaffected

Affected

A

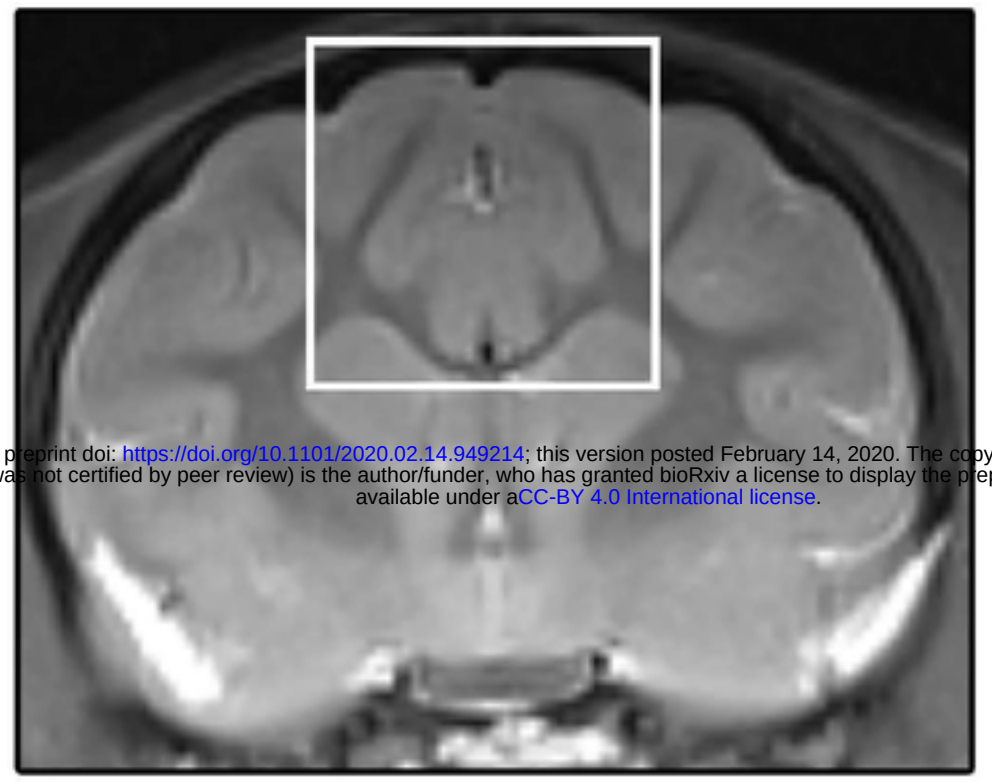

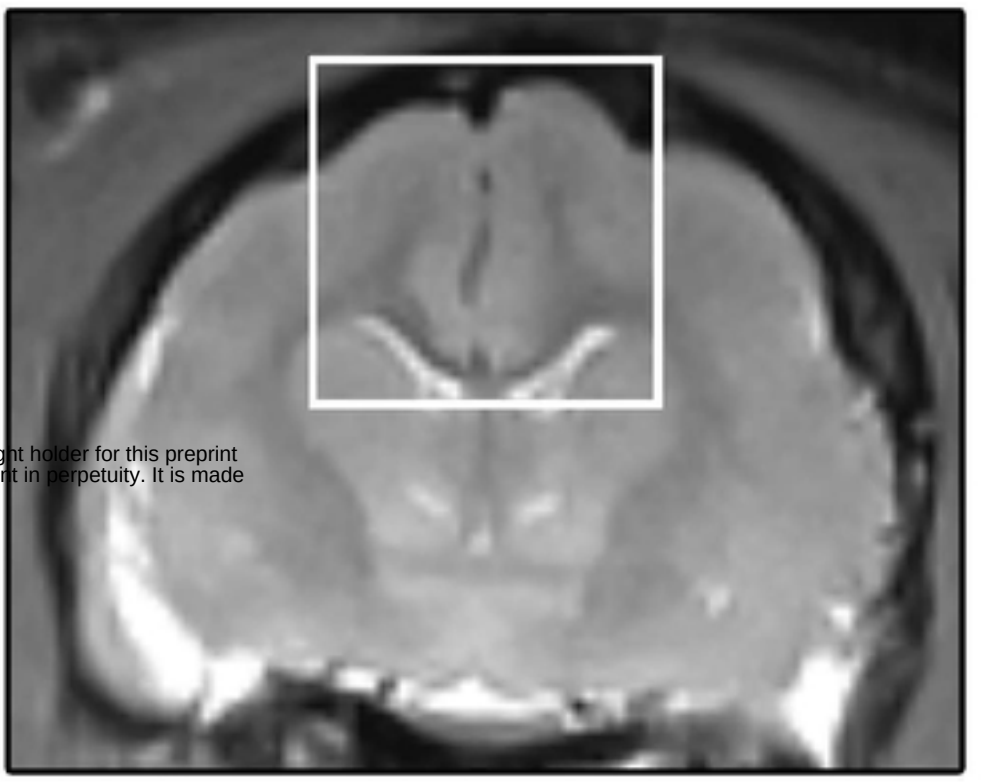

B

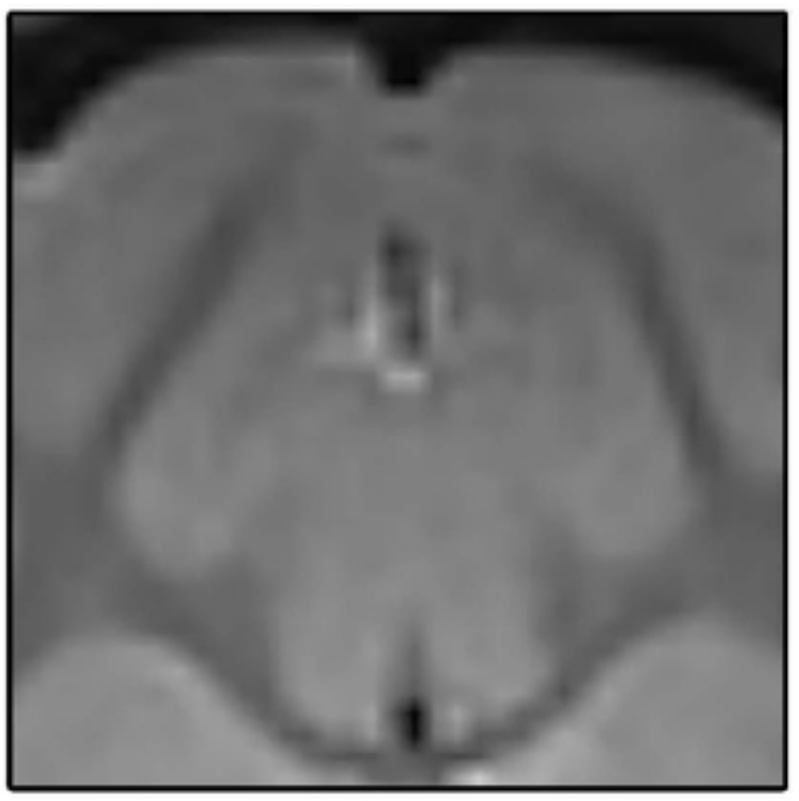

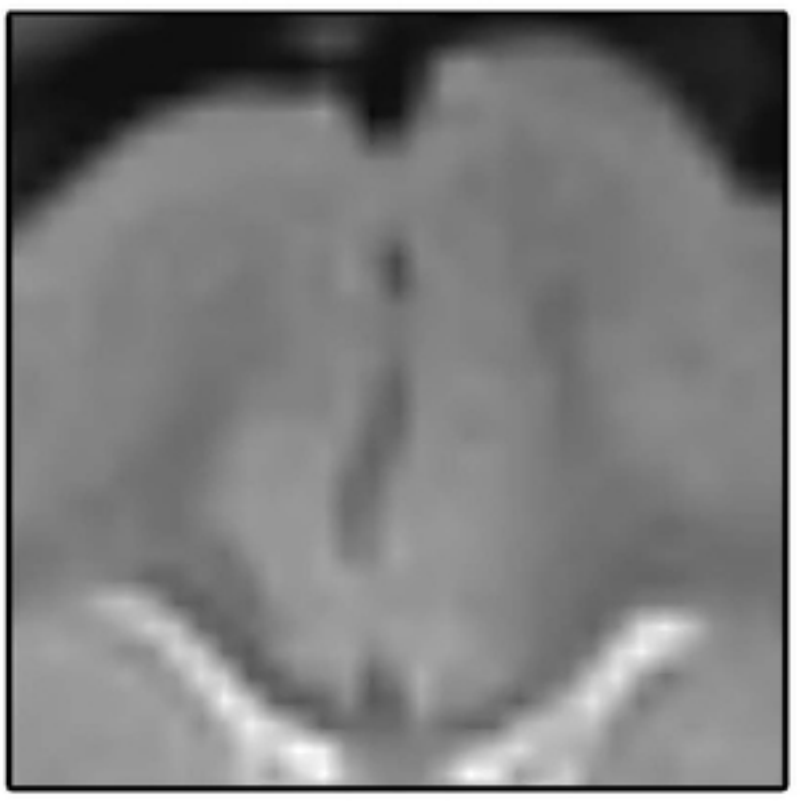

C

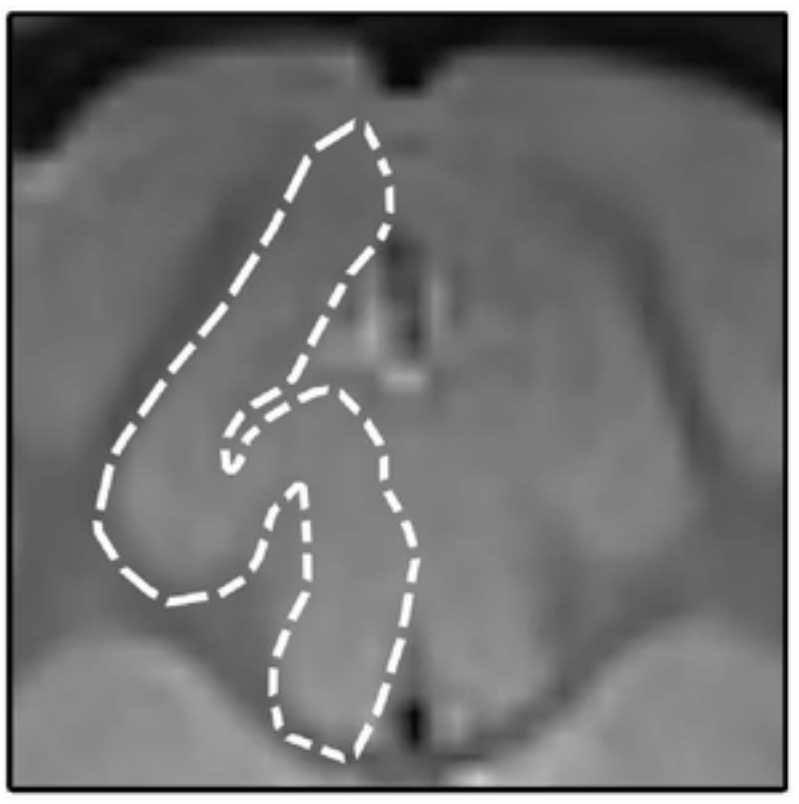

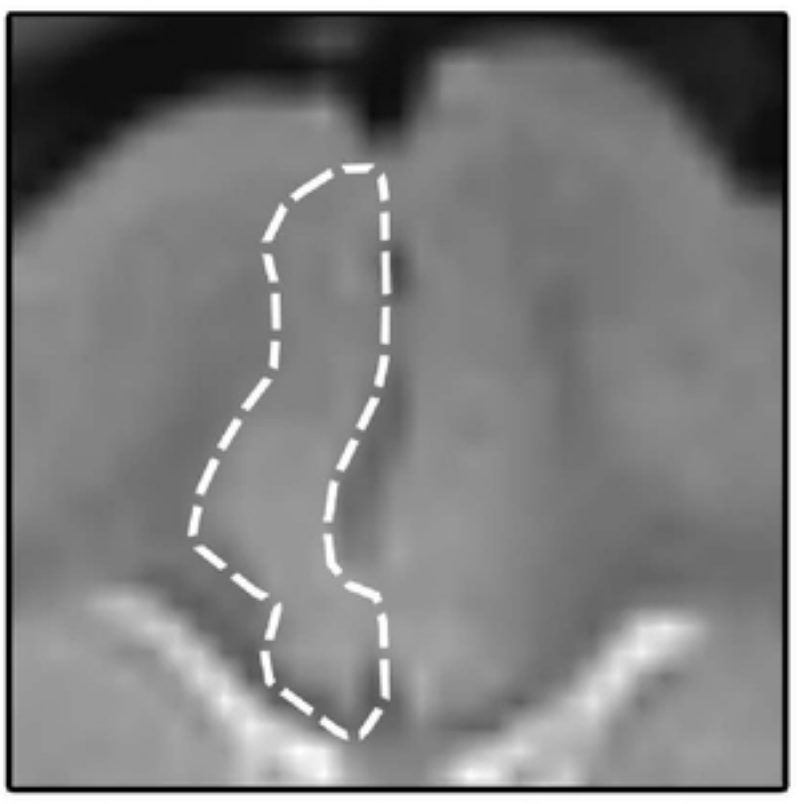

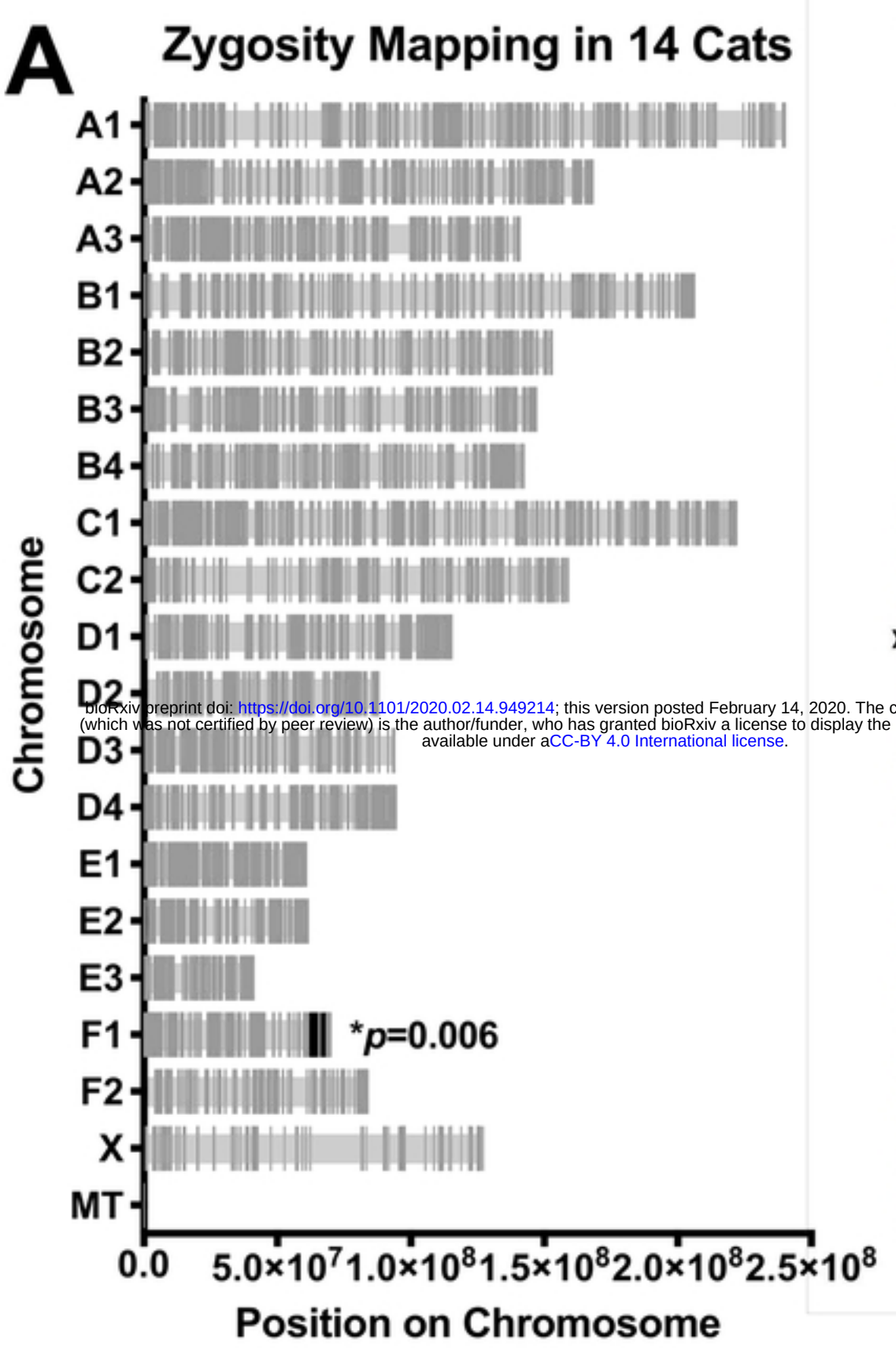

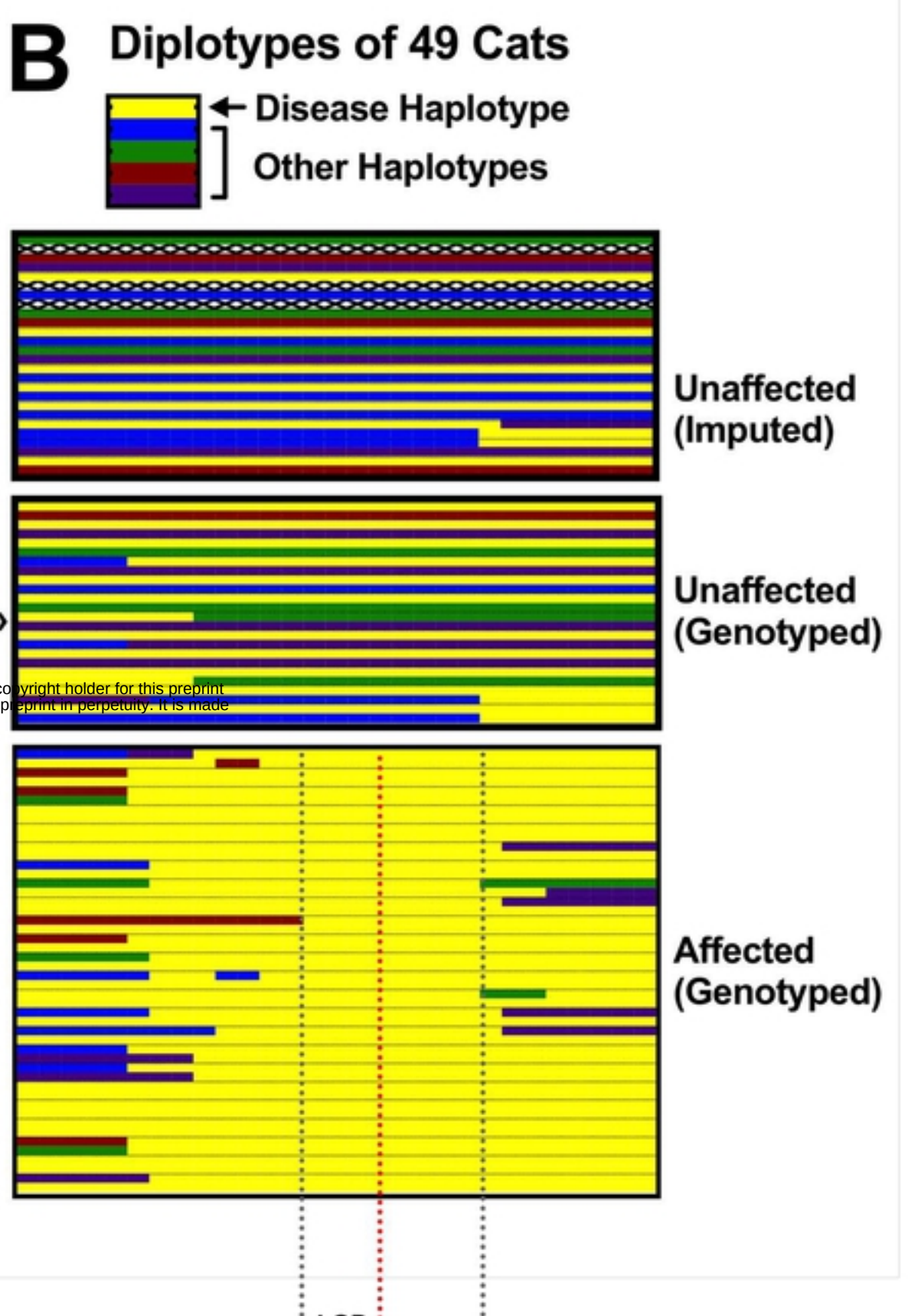

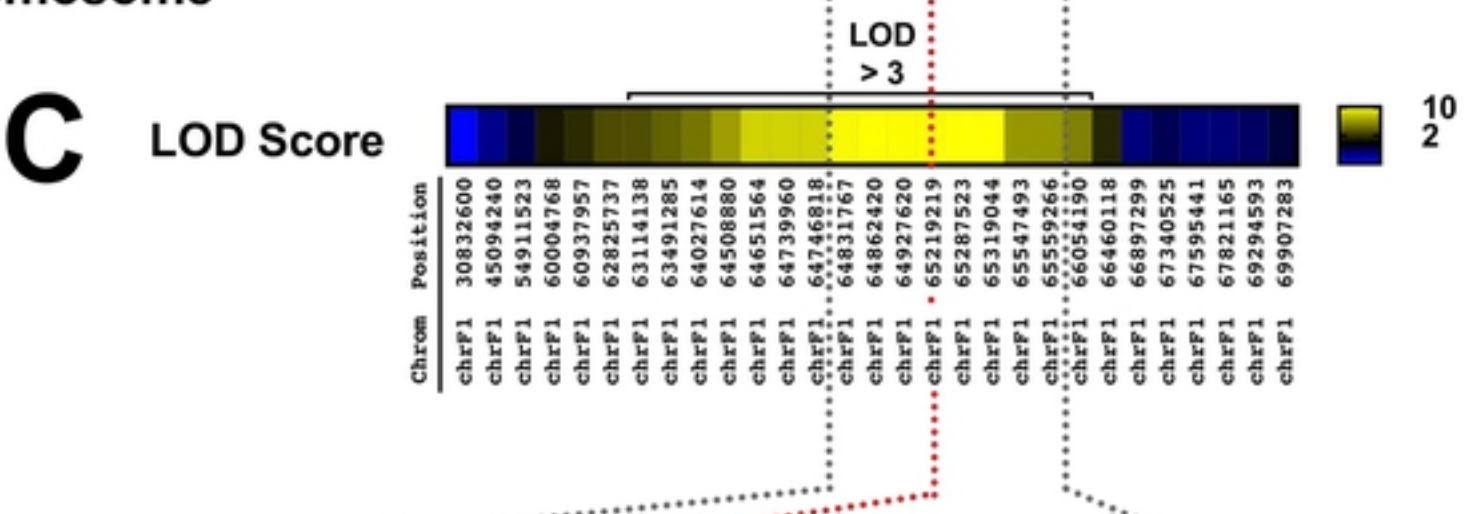

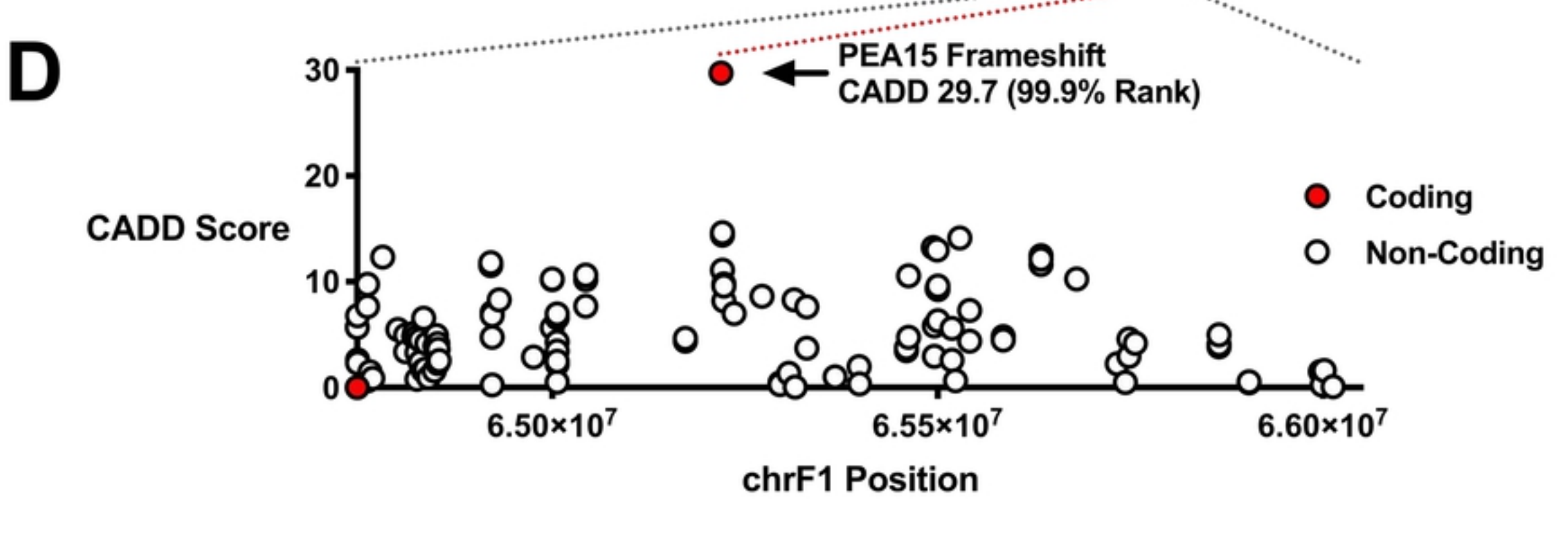

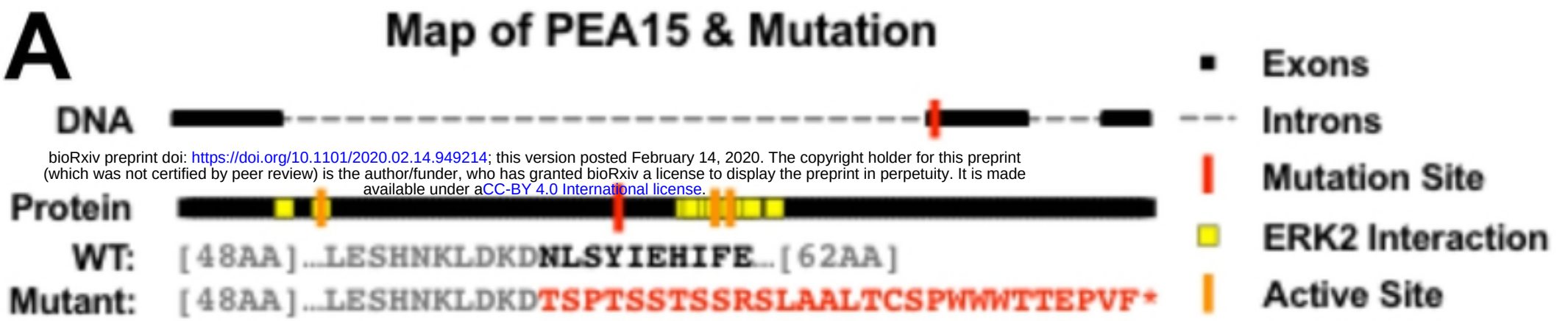

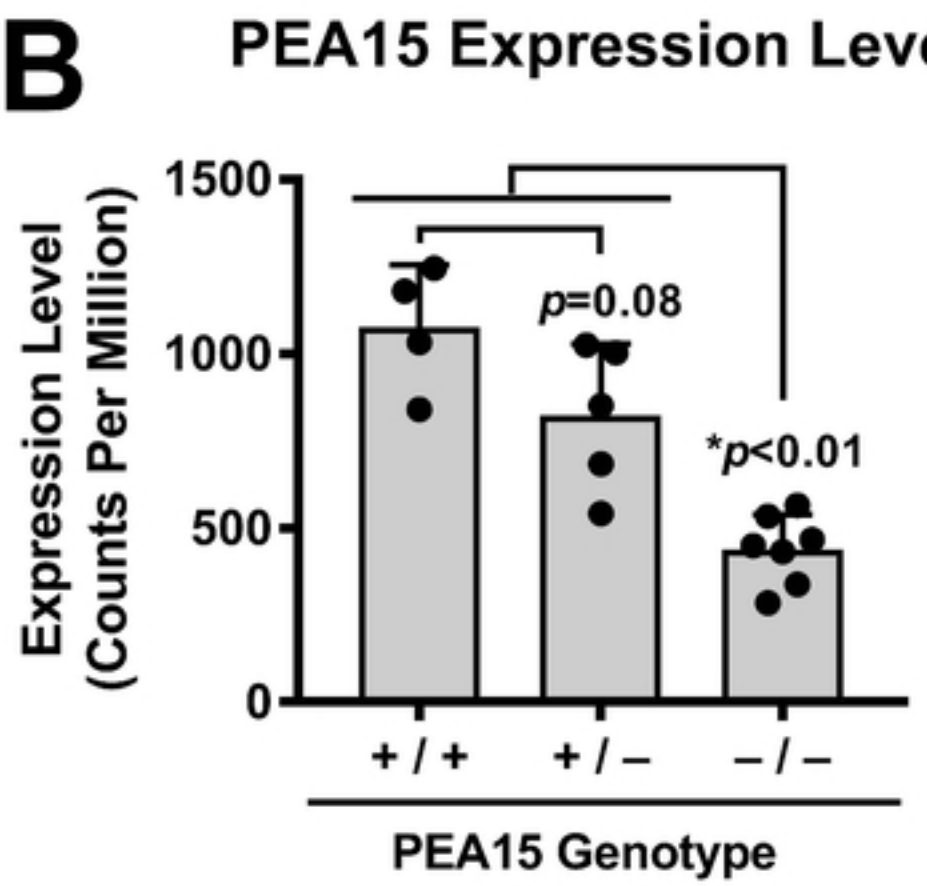

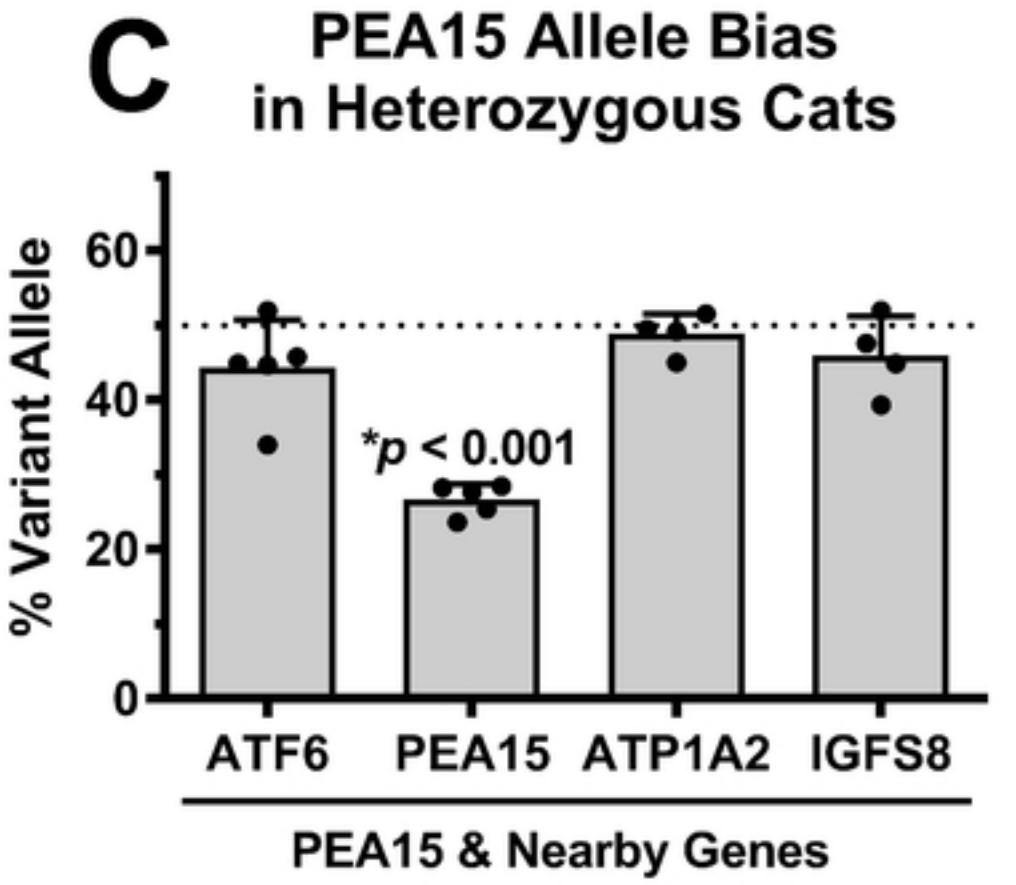

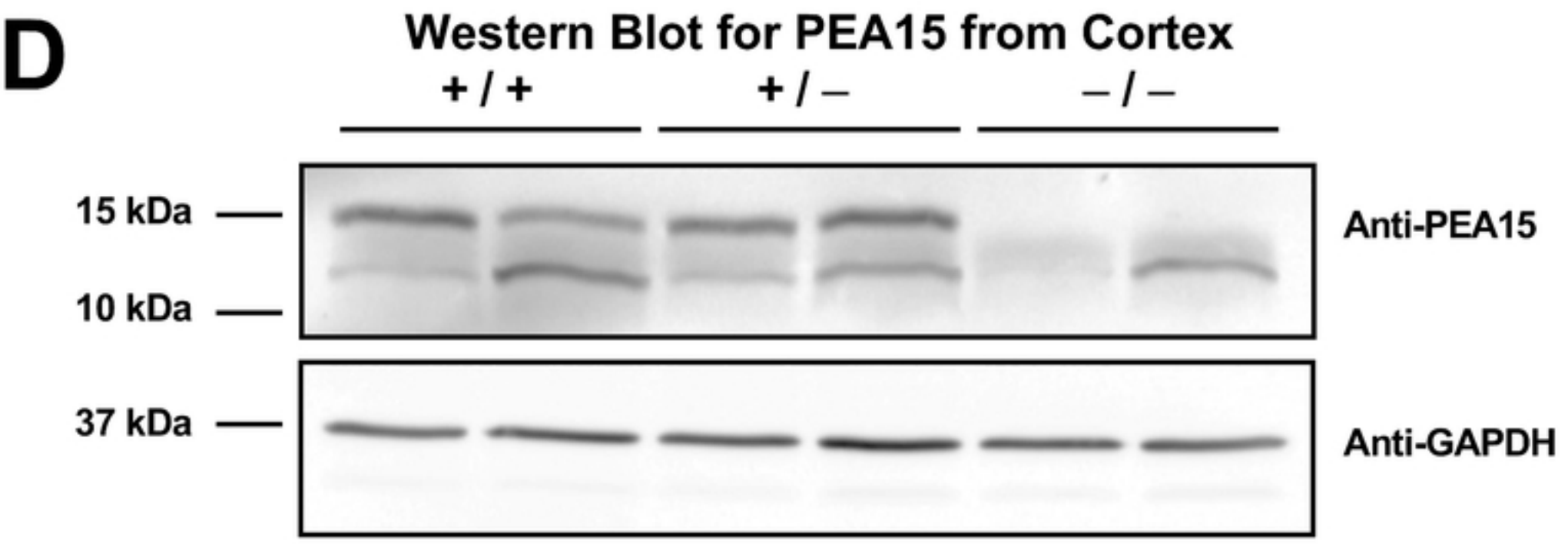

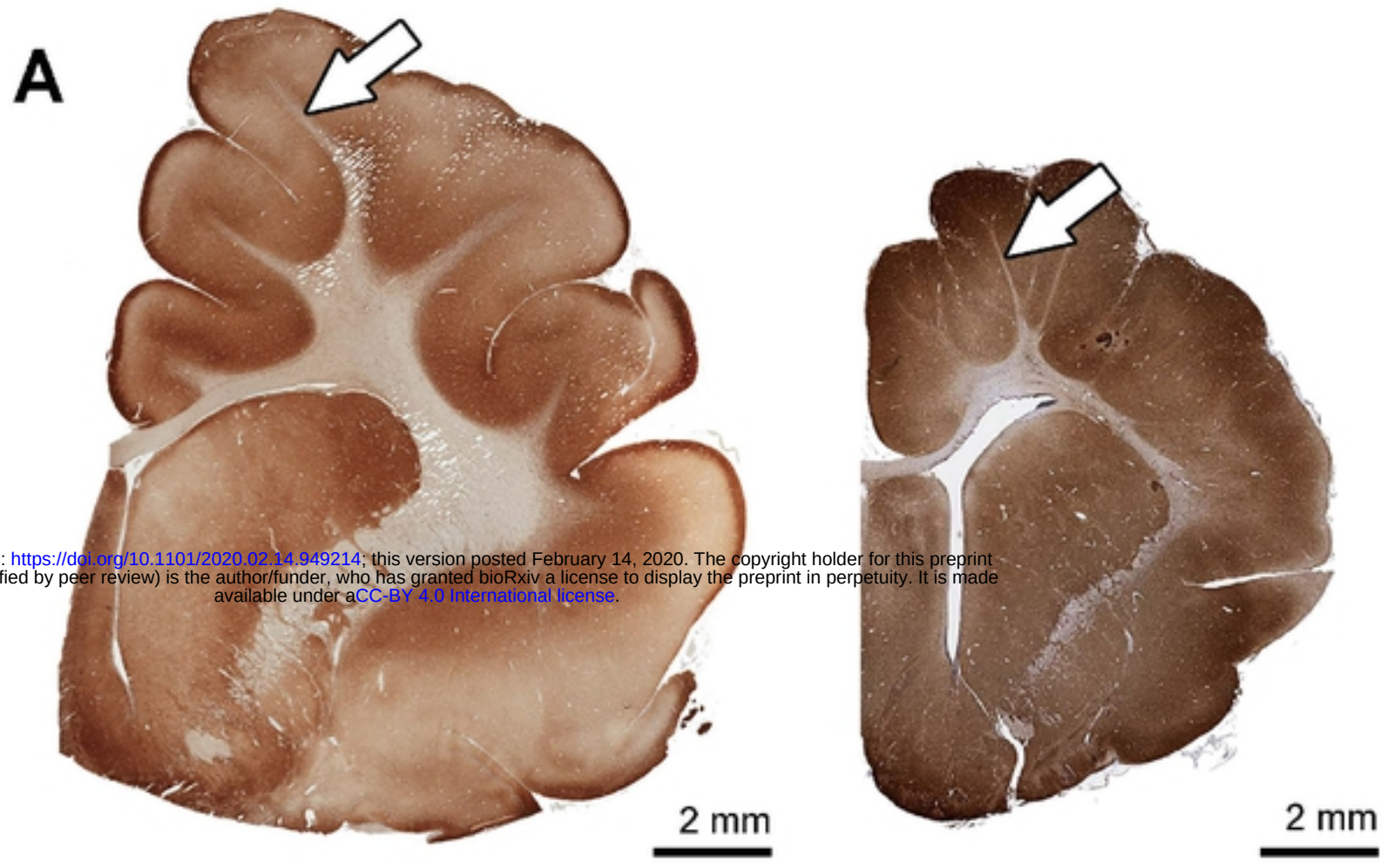

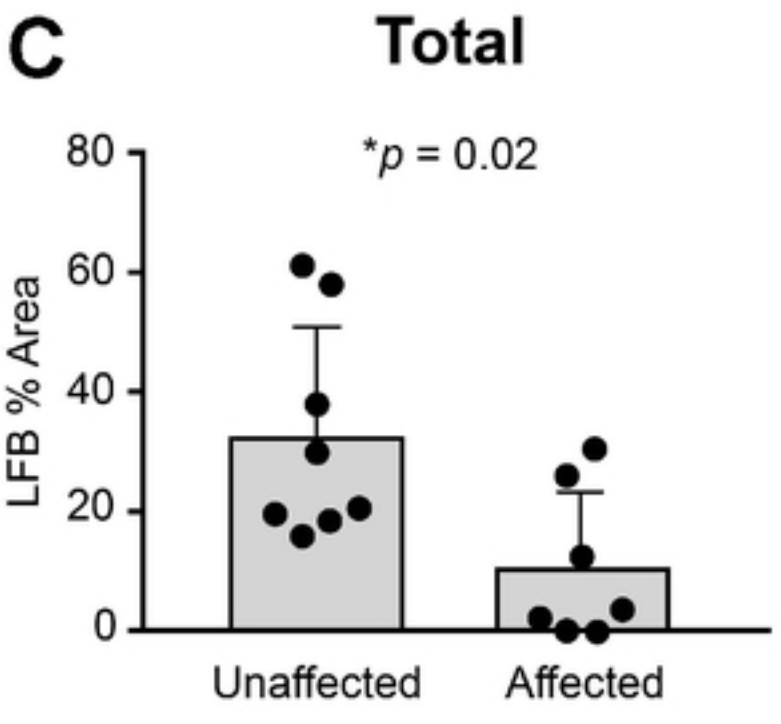

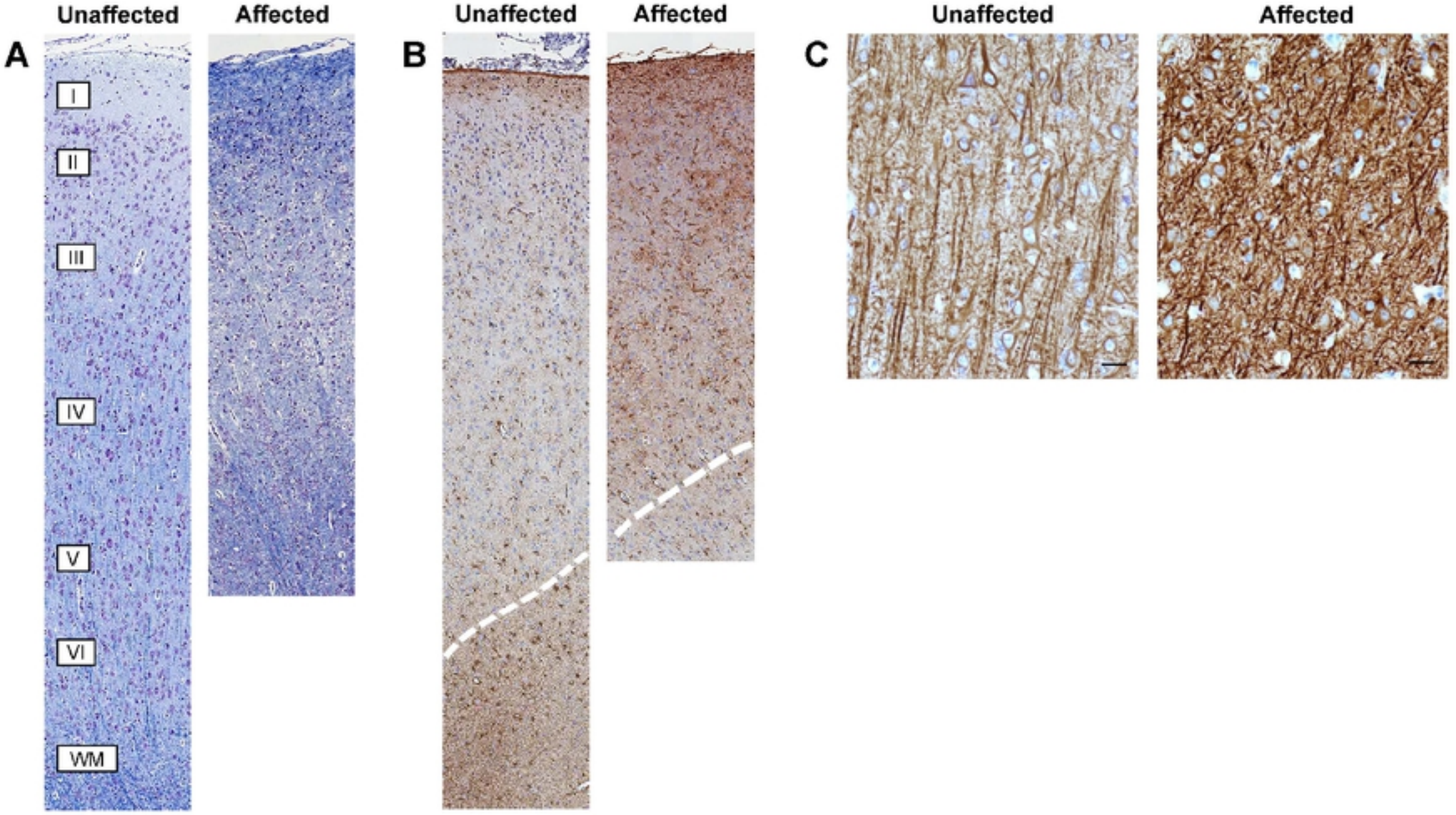
Unaffected
Affected
A
I
II
III
IV
V
VI
WM
Unaffected
Affected
B
Unaffected
Affected
C

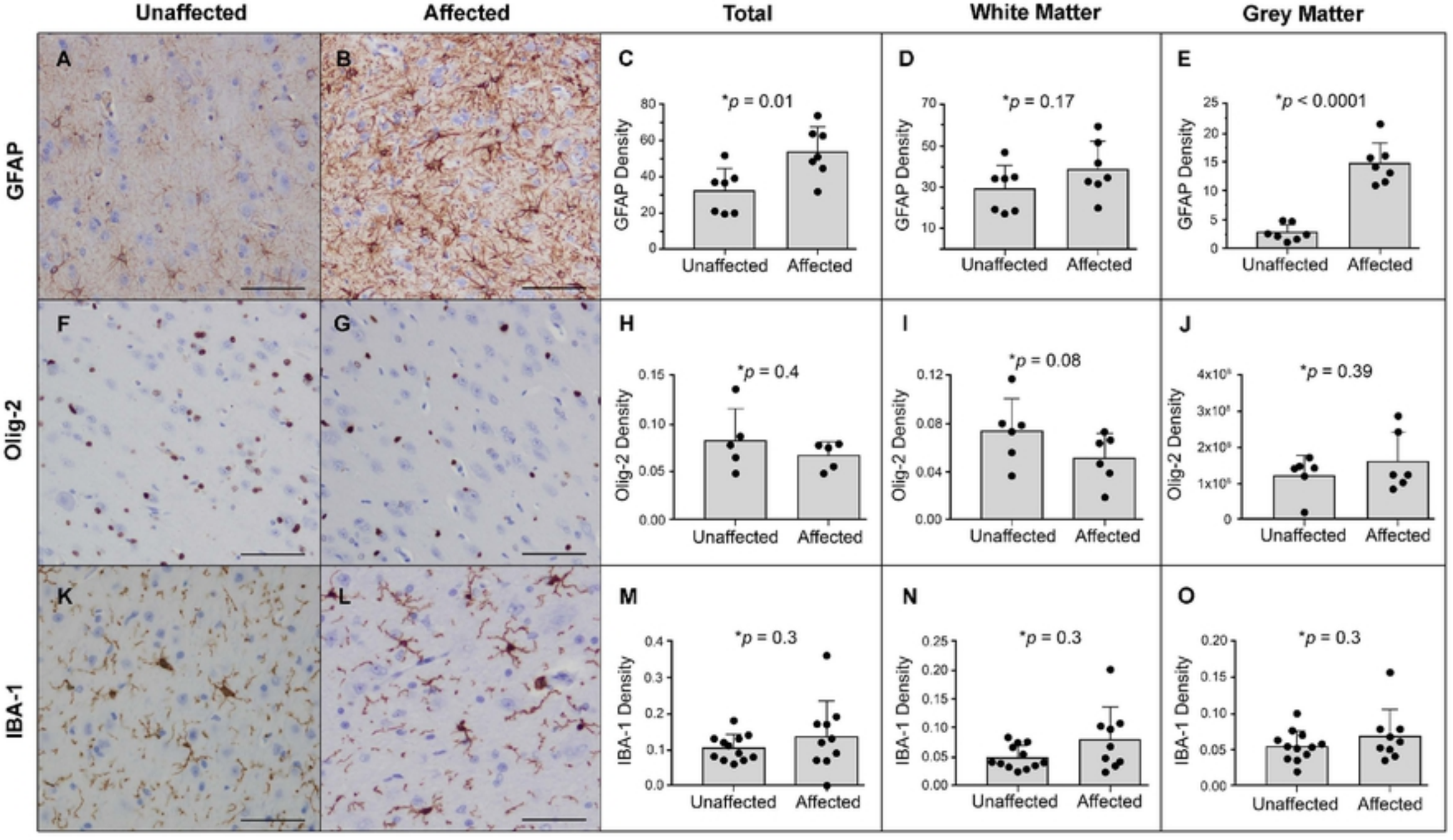
Unaffected
Affected
Total
White Matter
Grey Matter
GFAP
Olig-2
IBA-1
A
B
C
D
E
F
G
H
I
J
K
L
M
N
O
GFAP Density
Olig-2 Density
IBA-1 Density
*p = 0.01
*p = 0.17
*p < 0.0001
*p = 0.4
*p = 0.08
*p = 0.39
*p = 0.3
*p = 0.3
*p = 0.3
Unaffected
Affected

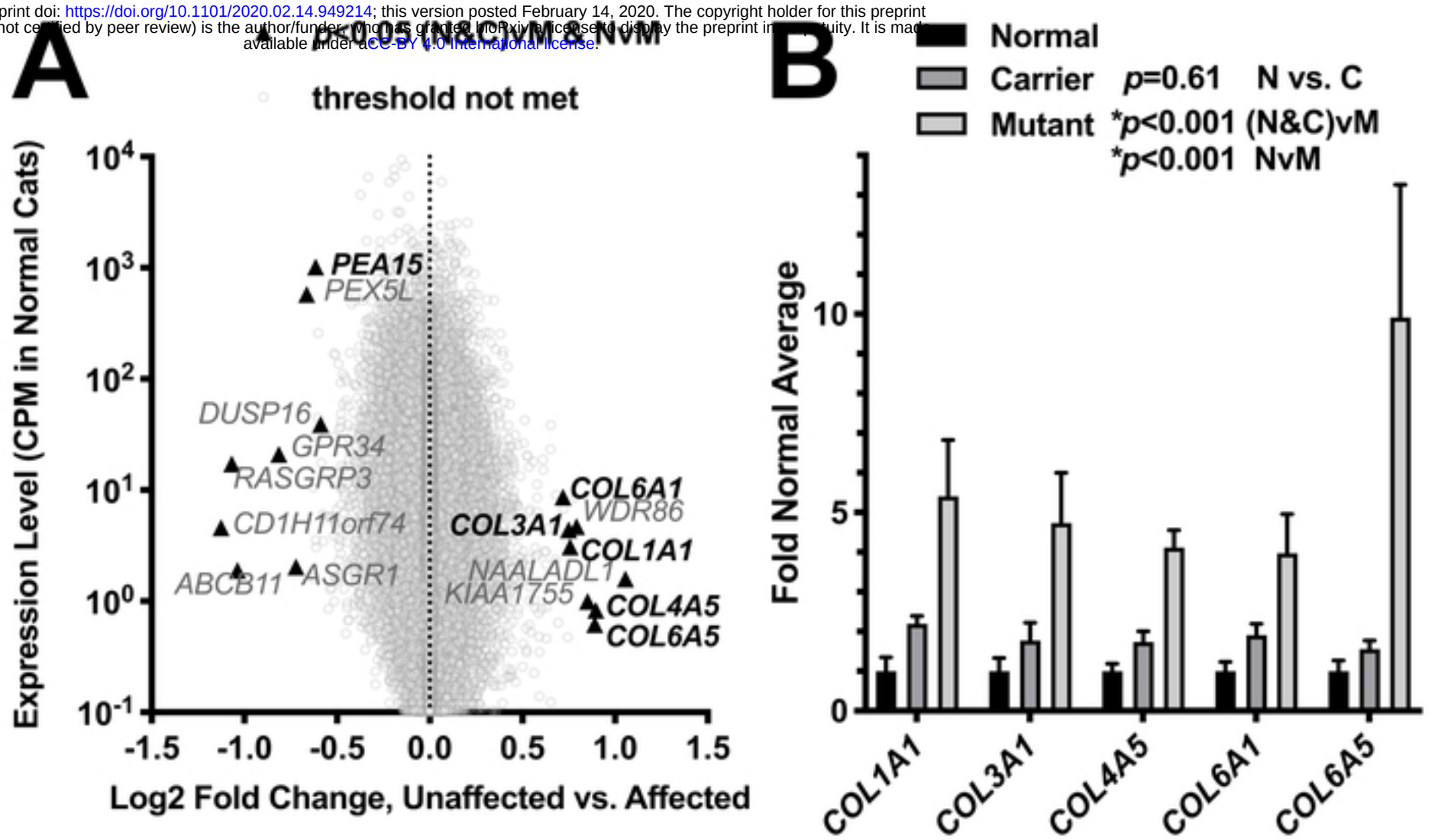

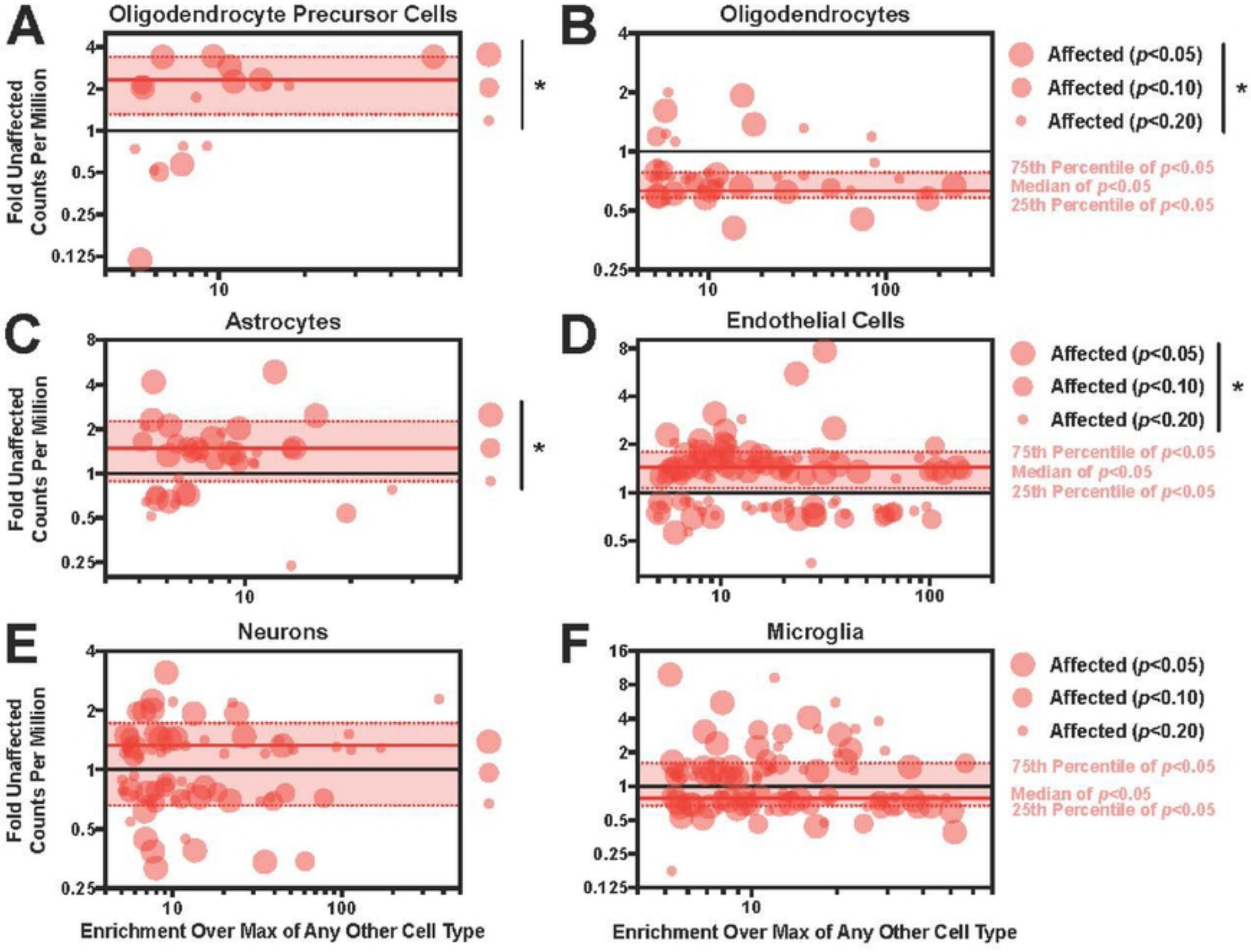
A
Oligodendrocyte Precursor Cells
B
Oligodendrocytes
C
Astrocytes
D
Endothelial Cells
E
Neurons
F
Microglia
Fold Unaffected Counts Per Million
Enrichment Over Max of Any Other Cell Type
Affected (p<0.05)
Affected (p<0.10)
Affected (p<0.20)
*
75th Percentile of p<0.05
Median of p<0.05
25th Percentile of p<0.05

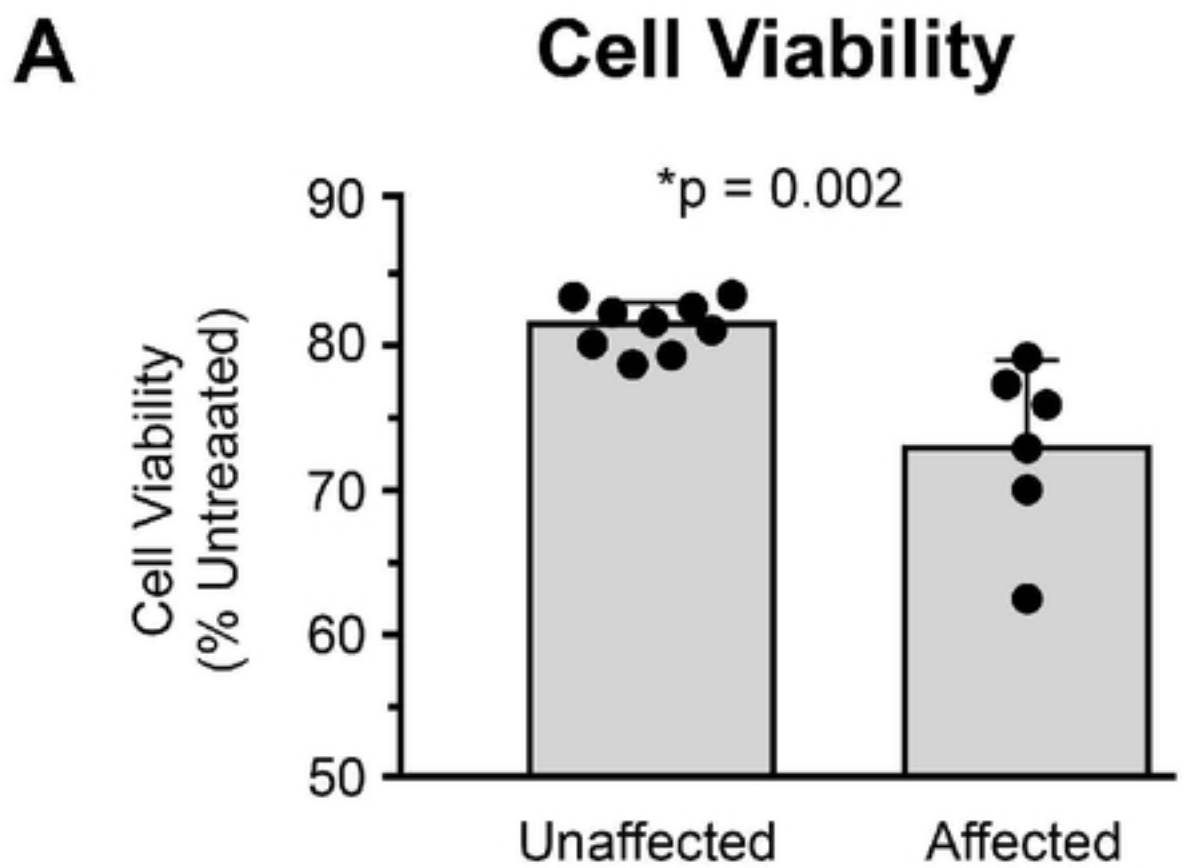

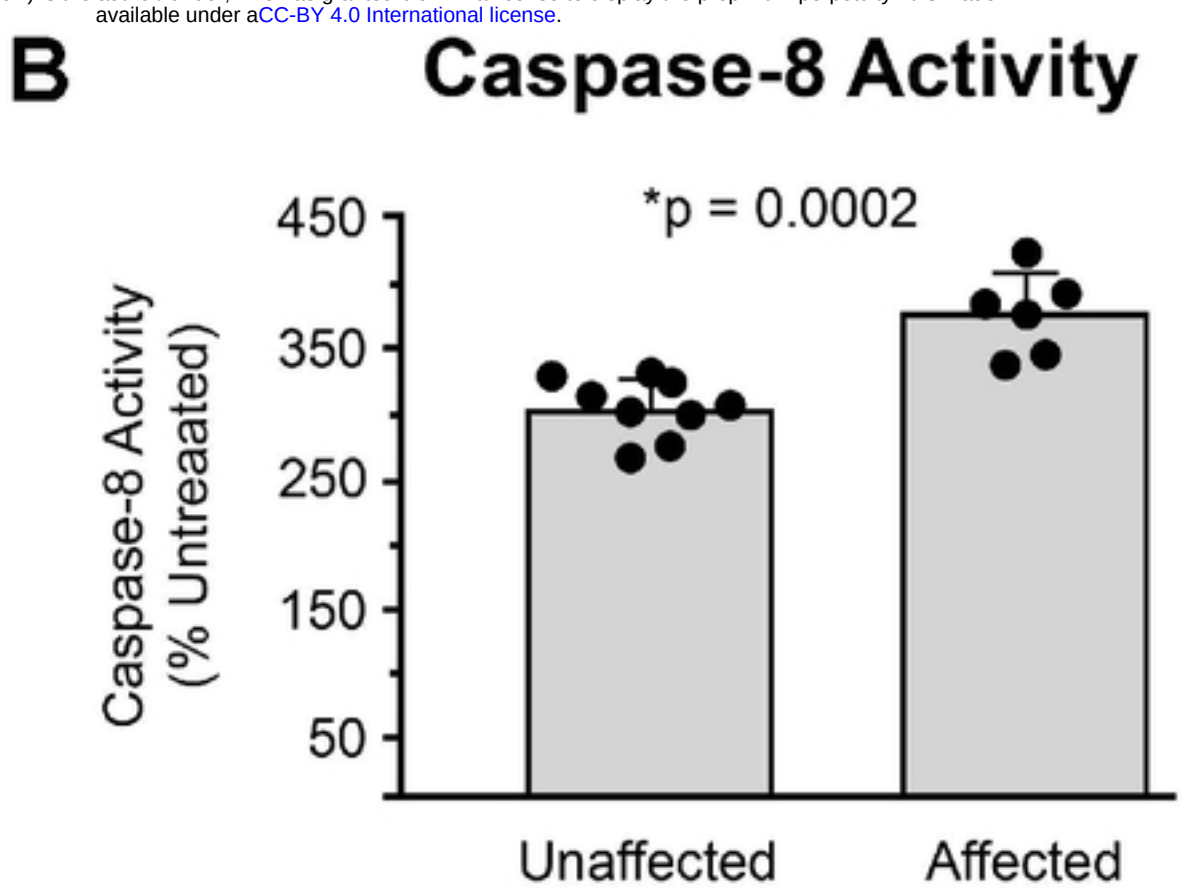

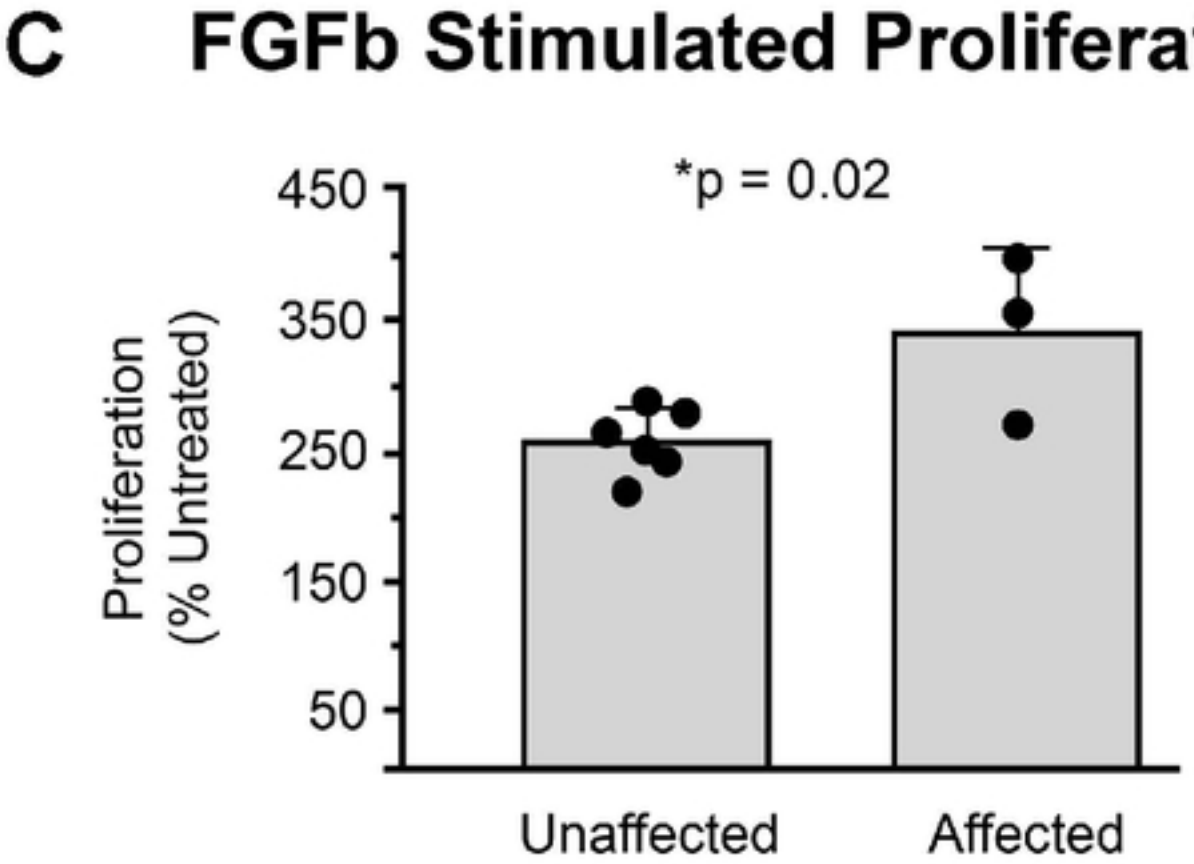

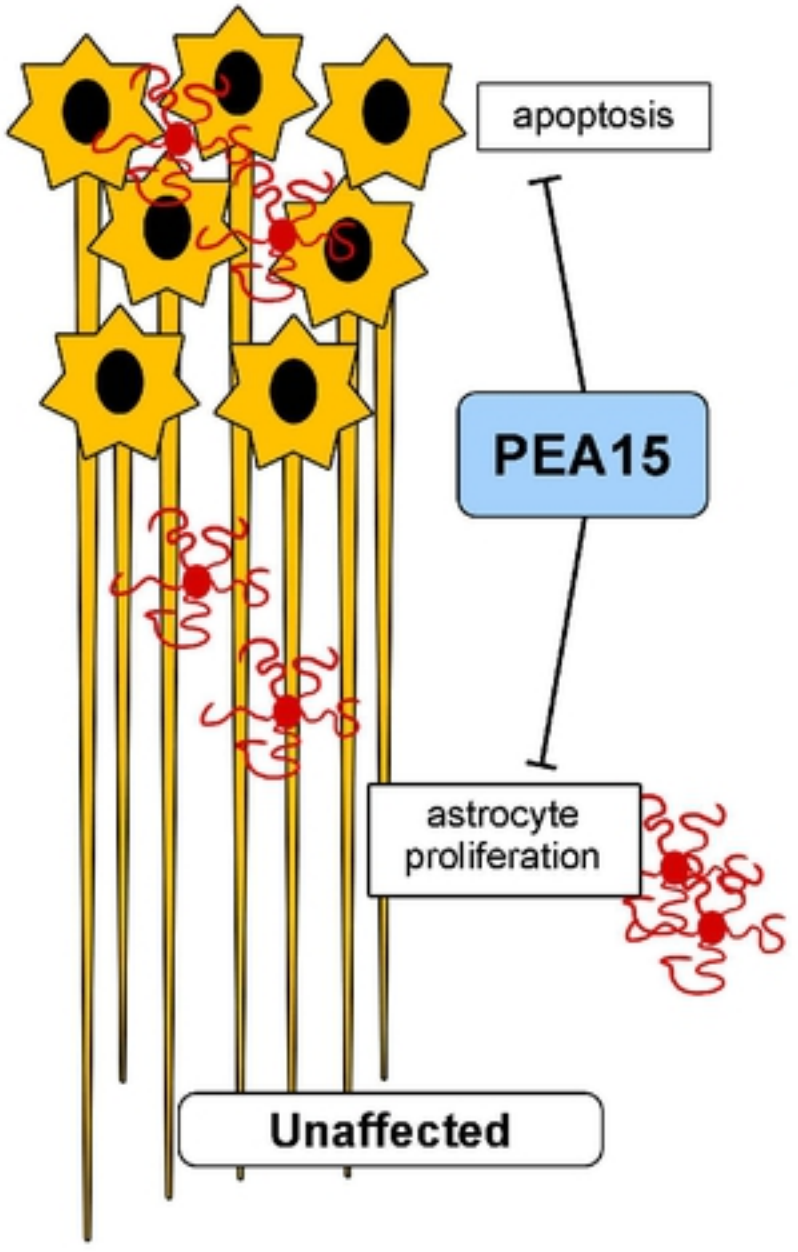

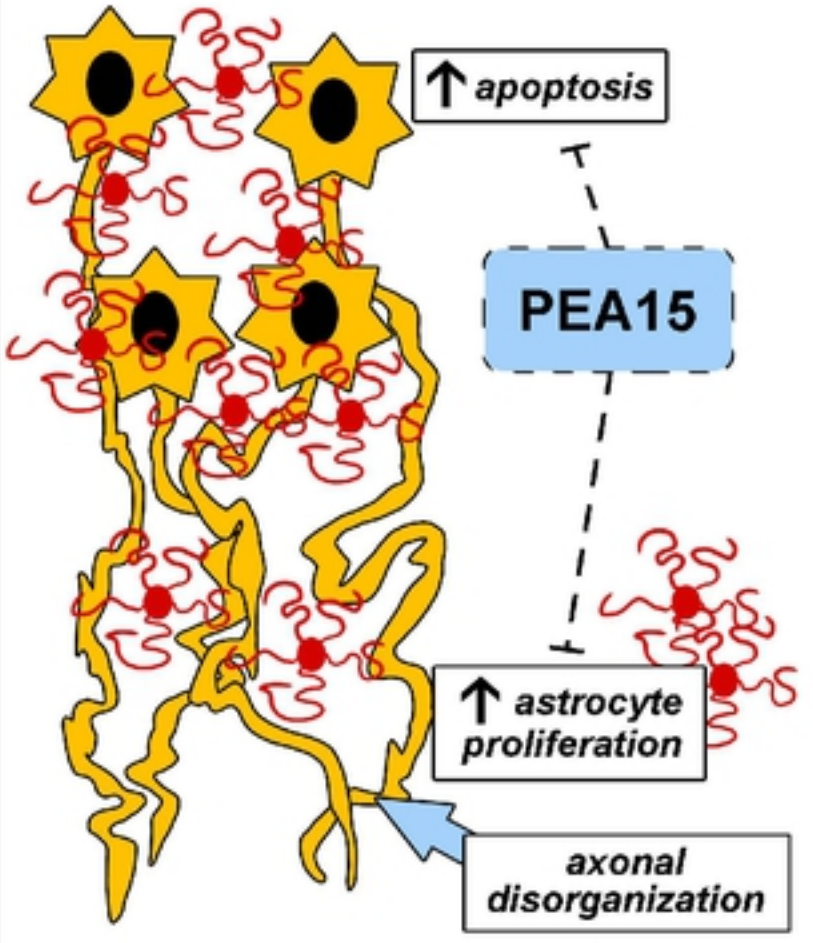

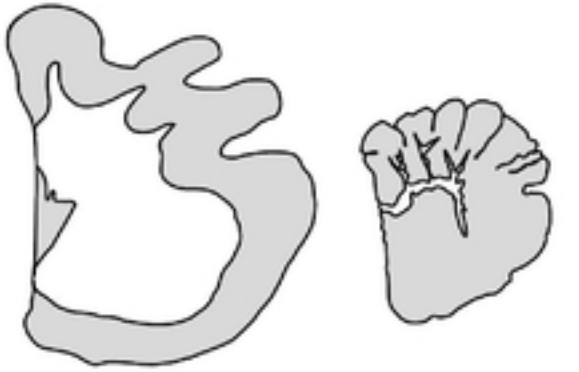

SUMMARY

During neurodevelopment, PEA15 regulates apoptosis and proliferation

↓

Absence of PEA15 leads to increased neuronal apoptosis and astrocyte proliferation

↓

Results in disorganized axonal development, underdeveloped white matter, microcephaly, and polymicrogyria